Supporting Information for

Reducing Energy Disorder in Perovskite Solar Cells by Chelation

Yiting Jiang,[†] Jiabin Wang,[‖] Huachao Zai,[†] Dongyuan Ni,[#] Jiayu Wang,[†] Peiyao Xue,[†] Nengxu Li,[†] Boyu Jia,[†] Huanjun Lu,[‖,±] Yu Zhang,[†] Feng Wang,[†] Zhenyu Guo,[†] Zhaozhao Bi,[§] Haipeng Xie,[‡] Qian Wang,[#] Wei Ma,[§] Yingfeng Tu,[‖,*] Huanping Zhou,[†,*] and Xiaowei Zhan[†,*]

[†] Key Laboratory of Polymer Chemistry and Physics of Ministry of Education, School of Materials Science and Engineering, Peking University, Beijing 100871, China

[‖] State and Local Joint Engineering Laboratory for Novel Functional Polymeric Materials, College of Chemistry, Chemical Engineering and Materials Science, Soochow University, Suzhou 215123, China

[#] Center for Applied Physics and Technology, School of Materials Science and Engineering, Peking University, Beijing 100871, China

[±] Jiangsu Key Laboratory of Micro and Nano Heat Fluid Flow Technology and Energy Application, School of Physical Science and Technology, Suzhou University of Science and Technology, Suzhou 215009, China

[§] State Key Laboratory for Mechanical Behavior of Materials, Xi'an Jiaotong University, Xi'an 710049, China

[‡] Hunan Key Laboratory for Super-microstructure and Ultrafast Process, School of Physics and Electronics, Central South University, Changsha 410012, China

Syntheses

Materials. 1,8-Octanediol (99%), 1,12-dodecanediol (99%) and *p*-toluenesulfonic acid (PTSA, 99%) are from J&K Chemical. 4-chlorobutyl acetate (98%), 4-hydroxybenzaldehyde (98%), 2-acetyl pyridine (98%), 4-(dimethylamino)pyridine (DMAP, 99%), *N*,*N*-diisopropylcarbodiimide (DIPC, 99%) and 1,2-dichlorobenzene (99%) are from Alfa Aesar. K_2CO_3 (chemically pure), Na_2SO_4 (chemically pure), KOH (chemically pure), NaOH (chemically pure), NaCl (chemically pure), hydrochloric acid (35%), hydrobromic acid (48%), ammonia solution (25%), trifluoroacetic acid (chemically pure), petroleum ether (chemically pure), diethyl ether (chemically pure), ethyl acetate (chemically pure), acetone (chemically pure), pyridine (chemically pure) and *N*,*N*-dimethylformamide (DMF, analytical reagent) are from Sinopharm Chemical Reagent Co., Ltd (China). [60]Fullerene (99.9%) is from Yongxin Technology Co., Ltd (China). All these chemicals were used as received. [60]Fullerenoacetic acid,[S1,S2] 4-(4-hydroxybutoxy) benzaldehyde (C4),[S3] 4-(8-hydroxyoctyloxy) benzaldehyde (C8)[S3] and 4-(12-hydroxydodecyloxy) benzaldehyde (C12)[S3] were synthesized according to reported methods.

DMF (99.99%, Sigma-Aldrich), dimethyl sulfoxide (DMSO, 99.5%, Sigma-Aldrich), chlorobenzene (CB, 99.9%, Sigma-Aldrich), 1,2-dichlorobenzene (DCB, 99.9%, Acros), toluene (AR, Beijing Tong Guang Fine Chemicals Corp.), methanol (HPLC grade, Tianjin Concord Technology Corp.), PbI_2 (99.99%, Xi'an Polymer Light Technology Corp.), $PbBr_2$ (99.999%, Sigma-Aldrich), CsI (99.9%,

Sigma-Aldrich), MABr (99.5%, Xi'an Polymer Light Technology Corp.), poly(triarylamine) (PTAA, 99%, Xi'an Polymer Light Technology Corp.), 2,3,5,6-tetrafluoro-7,7,8,8-tetracyanoquinodimethane (F4-TCNQ, 99%, Luminescence Technology Corp.), poly[(9,9-bis(*N*,*N*-dimethyl-*N*-ethylaminopropyl)fluorene-2,7-diyl)-*alt*-(9,9-dioctylfluorene-2,7-diyl)] dibromide (PFN-Br, 99%, Solarmer), phenyl-C61-butyric acid methyl ester (PCBM, 99.9%, Xi'an Polymer Light Technology Corp.), C60 (99.9%, Xi'an Polymer Light Technology Corp.), 2,9-dimethyl-4,7-diphenyl-1,10-phenanthroline (BCP, 99.9%, Xi'an Polymer Light Technology Corp.) and indium tin oxide glass (ITO, Advanced Election Technology Corp.) were used as received. FAI and MACl were synthesized according to the reported methods.[S4]

Synthesis of P-C12. A mixture of 2-acetyl pyridine (1.3 g, 10.7 mmol), C12 (1.0 g, 3.3 mmol) and NaOH (0.8 g) in ethanol (30 mL) was stirred at 25 ℃ for 12 h, then 25% ammonia solution (15 mL) was added, and the solution was heated up to 65 ℃, stirred for 24 h, then cooled to room temperature and filtered. The residue was washed with ethanol, recrystallized in toluene, filtered and dried under vacuum to obtain a white solid 140 mg (with a yield of 85%). ^{1}H NMR (400 MHz, *d*-DMSO): δ (ppm) 8.76 (d, J = 4.0 Hz, 2H), 8.68 (s, 2H), 8.66 (s, 2H), 8.04 (t, J = 7.6 Hz, 2H), 7.87 (d, J = 8.8 Hz, 2H), 7.53 (t, J = 5.2 Hz, 2H), 7.12 (d, J = 8.4 Hz, 2H), 4.34 (t, J = 4.8 Hz, 1H), 4.05 (t, J = 6.0 Hz, 2H), 3.38 (q, J = 5.4 Hz, 2H), 1.73-1.77 (m, 2H), 1.25-1.42 (m, 18H). MALDI-TOF: calc. for $C_{33}H_{39}O_2N_3$: 509.682 $(M)^+$. Found: 510.413.

Synthesis of P-C4. Compounds P-C4 was synthesized with the similar procedure of P-C12 using corresponding C4 as reactant. ^{1}H NMR (400 MHz, *d*-DMSO): δ (ppm) 8.76 (d, *J* = 4.0 Hz, 2H), 8.68 (s, 2H), 8.65 (s, 2H), 8.03 (t, *J* = 7.6 Hz, 2H), 7.87 (d, *J* = 8.0 Hz, 2H), 7.52 (t, *J* = 5.6 Hz, 2H), 7.12 (d, *J* = 8.0 Hz, 2H), 4.48 (t, *J* = 4.0 Hz, 1H), 4.07 (t, *J* = 6.0 Hz, 2H), 3.48 (q, *J* = 5.0 Hz, 2H), 1.76-1.83 (m, 2H), 1.56-1.63 (m, 2H). MALDI-TOF: calc. for $C_{25}H_{23}O_2N_3$: 397.460 $(M)^+$. Found: 398.015.

Synthesis of P-C8. Compounds P-C8 was synthesized with the similar procedure of P-C12 using corresponding C8 as reactant. ^{1}H NMR (400 MHz, *d*-DMSO): δ (ppm) 8.76 (d, *J* = 4.4 Hz, 2H), 8.68 (s, 2H), 8.65 (s, 2H), 8.03 (t, *J* = 7.6 Hz, 2H), 7.87 (d, *J* = 8.4 Hz, 2H), 7.52 (t, *J* = 5.6 Hz, 2H), 7.12 (d, *J* = 8.4 Hz, 2H), 4.33 (t, *J* = 5.2 Hz, 1H), 4.05 (t, *J* = 6.4 Hz, 2H), 3.37 (q, *J* = 5.2 Hz, 2H), 1.73-1.78 (m, 2H), 1.30-1.42 (m, 10H). MALDI-TOF: calc. for $C_{29}H_{31}O_2N_3$: 453.571 $(M)^+$. Found: 454.281.

Synthesis of FP-C12. To mixed solvent of 1,2-dichlorobenzene (4.6 mL) and DMF (1.3 mL), [60]fullerenoacetic acid (0.2 g, 0.26 mmol), P-C12 (0.2 g, 0.39 mmol), DMAP (0.1 g), PTSA (0.2 g) and DIPC (0.2 g) were added. After stirring at 25 ℃ for 4 h, the mixture was filtered, washed with toluene and deionized water and concentrated under reduced pressure. The crude product was purified by column chromatography on silica gel (eluent: toluene:ethyl acetate:pyridine = 10:2:1) and concentrated under reduced pressure. The residue was precipitated in methanol, filtered and dried under vacuum to obtain a kermesinus solid 264 mg (with a yield of

80%). ^{1}H NMR (400 MHz, $CDCl_3$): δ (ppm) 8.70-8.89 (m, 6H), 7.92-8.11 (m, 4H), 7.49 (t, J = 5.6 Hz, 2H), 7.04 (d, J = 8.4 Hz, 2H), 4.78 (s, 1H), 4.47 (t, J = 5.2 Hz, 2H), 4.03 (t, J = 6.4 Hz, 2H), 1.68-1.80 (m, 4H), 1.19-1.60 (m, 16H). MALDI-TOF: calc. for $C_{95}H_{39}O_3N_3$: $(M)^+$ 1270.375. Found: 1270.535.

Synthesis of FP-C4. FP-C4 was synthesized following the same procedure as FP-C12 using P-C4 as reactant. ^{1}H NMR (400 MHz, $CDCl_3$): δ (ppm) 8.68-8.97 (m, 6H), 7.92-8.12 (m, 4H), 7.49 (t, J = 6.0 Hz, 2H), 7.09 (d, J = 8.0 Hz, 2H), 4.71 (s, 1H), 4.59 (t, J = 5.6 Hz, 2H), 4.21 (t, J = 5.2 Hz, 2H), 2.02-2.19 (m, 2H), 1.18-1.32 (m, 2H). MALDI-TOF: calc. for $C_{87}H_{23}O_3N_3$: 1158.159 $(M)^+$. Found: 1158.369.

Synthesis of FP-C8. FP-C8 was synthesized following the same procedure as FP-C12 using P-C8 as reactant. ^{1}H NMR (400 MHz, $CDCl_3$): δ (ppm) 8.64-8.90 (m, 6H), 7.82-8.05 (m, 4H), 7.49 (t, J = 6.0 Hz, 2H), 7.10 (d, J = 8.8 Hz, 2H), 4.71 (s, 1H), 4.59 (t, J = 6.4 Hz, 2H), 4.02 (t, J = 6.4 Hz, 2H), 1.78-1.94 (m, 2H), 1.15-1.64 (m, 10H). MALDI-TOF: calc. for $C_{91}H_{31}O_3N_3$: 1214.267 $(M)^+$. Found: 1214.373.

The main cost of the fullerene derivatives is from the fullerene starting material due to its high price (~ 50 $ per gram for 99.9% [60]fullerene C60). Typically, the synthesis yield of methanofullerenes is around 50%, similar in the synthesis of PCBM[S5] and our [60]fullerenoacetic acid from C60. Since the yield of esterification of [60]fullerenoacetic acid with P-Cn is quite high (~80%), while the molecular weights of FP-Cn (1160~1270 Da) are larger than that of PCBM (910 Da), the synthetic cost of FP-Cn is comparable to that of PCBM.

Device Fabrication and Stability Tests

Device fabrication. Typical planar *p-i-n* perovskite solar cells (PSCs) with ITO/PTAA (F4-TCNQ doped)/PFN-Br/$Cs_{0.05}FA_{0.90}MA_{0.05}PbI_{2.85}Br_{0.15}$ (CsFAMA)/ETL/C60/BCP/ Ag structure were prepared as follows: ITO substrate was cleaned with ultra-pure water, ethanol and isopropanol, respectively. The ITO substrate was treated with UV ozone for 30 min and then was transferred into a N_2-filled glovebox (H_2O, O_2 < 0.1 ppm). A solution of PTAA (60 μL, 2 mg mL^{-1} in toluene, 10 wt% F4-TCNQ doped) was spin-coated onto the ITO substrate at 4000 rpm for 25 s and then annealed at 120 ℃ for 10 min. After the PTAA-coated ITO was cooled down to room temperature, a 60 μL solution of PFN-Br (0.5 mg mL^{-1} in methanol) was spin-coated onto the PTAA layer at 5000 rpm for 20 s and annealed at 120 ℃ for 1 min. The perovskite solution was prepared by mixing 217.28 mg FAI, 612.34 mg PbI_2, 7.45 mg MABr, 26.33 mg $PbBr_2$ and 18.20 mg CsI in 1 mL DMF/DMSO mixed solvent (4:1, v:v), 9.45 mg MACl was added into the perovskite solution and stirred overnight for fully dissolved. 35 μL of the prepared perovskite solution was spin-coated onto the ITO/PTAA/PFN-Br substrate at 1000 rpm for 10 s and 5000 rpm for 30 s. 200 μL CB was dropped onto the spinning substrate at 10 s before the end of the procedure. Subsequently, the perovskite film was annealed at 120 ℃ for 1 h. After that, 30 μL of PCBM or FP-Cn (20 mg mL^{-1} in DCB) was spin-coated onto the perovskite film at 3000 rpm for 30 s and annealed at 70 ℃ for 10 min. Finally, 15 nm C60, 6 nm BCP and 120 nm silver electrode were evaporated on the top of ETL under a pressure of 1×10^{-5} Pa, successively. The $FAPbI_3$ based PSCs

were fabricated with ITO/PTAA/$FAPbI_3$/ETL/C60/BCP/Cu structure, where perovskite layer was deposited by a two-step method, and the other process is similar to the former one. Noted that most of characterizations were conducted based on the CsFAMA perovskite to verify the validity of molecular chelation strategy, and the $FAPbI_3$ perovskite was employed to prove the universality of the chelation strategy and to obtain a higher device efficiency.

Stability tests. The thermal stability tests were conducted in a N_2-filled glovebox, and the devices were kept under dark and put on a hot-plate with a continuous heating at 65 ℃. The shelf stability tests were carried out in ambient atmosphere with relative humidity (RH) of 20-60%, temperature at 20-30 ℃, and the devices were stored in dark. The operating stability tests were conducted under continuous light irradiation and stabilized power output (SPO) tracking with constant 0.8 V applied bias voltage by using a white LED lamp (100 mW cm^{-2}) in N_2-filled glovebox, and the temperature was kept at about 40 ℃. All the aging tests were carried out in N_2-filled glovebox, and the ETL films were kept facing up for the light soaking process. All devices or films employed were unencapsulated, and the water or oxygen concentration of glovebox was below 0.1 ppm during 65 ℃ heating or SPO tracking.

Characterizations

Proton nuclear magnetic resonance (^{1}H NMR) spectroscopy. The ^{1}H NMR spectra were collected with an Agilent Direct-Drive Π 400 MHz NMR spectrometer

(^{1}H Larmor frequency: 400 MHz). The chemical shifts (δ values) were tested in parts per million (ppm) down-field, and the internal reference was tetramethylsilane (TMS).

Matrix-assisted laser desorption/ionization time of flight (MALDI-TOF) mass spectroscopy. MALDI-TOF mass spectra were conducted on a GCT-Primier mass spectrometer. Trans-2-[3-(4-tert-butylphenyl)-2-methyl-2-propenylidene]malononitrile (DCTB) was served as matrix and with a concentration of 20 mg mL^{-1} $CHCl_3$. Sodium iodide (NaI) served as cationizing agent and with a concentration of 10 mg mL^{-1} methanol.

Cyclic voltammetry measurements. The electrochemical measurements were carried out under N_2 on a deoxygenated solution of 0.1 M tetra-n-butylammonium hexafluorophosphate ($[Bu_4N]^+[PF_6]^-$) in CH_3CN using a computer-controlled CHI660E electrochemical workstation, with a glassy-carbon working electrode to carry samples, an Ag/AgCl reference electrode, and a platinum-wire auxiliary electrode. Potentials were referenced to ferrocenium/ferrocene ($FeCp_2^{0/+}$) couple by using ferrocene as an internal standard.

Ultraviolet photoelectron spectroscopy/X-ray photoelectron spectroscopy (UPS/XPS). UPS and XPS measurements were conducted on an XPS AXIS Ultra DLD (Kratos Analytical).

Scanning electron microscopy (SEM). The SEM of perovskite thin films and cross-sectional SEM images of device were captured with cold field-emission scanning electron microscope (Hitachi S4800).

Atomic force microscopy (AFM). AFM measurements were performed on a Dimension Icon, Bruker, using standard mode.

Contact angle measurements. Contact angle measurements were carried out on a Dataphysics OCA20 contact-angle system at ambient temperature (the test liquid is water).

Grazing incidence wide-angle X-ray scattering (GIWAXS). GIWAXS measurements were performed at beamline 7.3.3[S6] at the advanced light source. Samples were prepared on Si substrates using identical blend solutions as those used in devices. The 10 keV X-ray beam was incident at a grazing angle of 0.12 °-0.16 °, selected to maximize the scattering intensity from the samples. The scattered x-rays were detected using a Dectris Pilatus 2M photon counting detector.

Fourier transform infrared (FTIR) spectroscopy. Samples were prepared with KBr powder, and FTIR spectra were measured using Fourier transform infrared spectrometer (Tensor 27, Germany Bruker).

Ultraviolet-visible (UV-vis) spectroscopy. The UV-vis absorption spectra were obtained using UV–vis diffuse reflectance spectrophotometer (Hitachi UH4150). The bandgap of perovskite was obtained by fitting the x-axis of the linear region of the Tauc plot, which can be derived from UV-vis spectrum in $(\alpha h\nu)^2$ vs. $h\nu$ representation, where α is the absorption coefficient, and $h\nu$ is the energy of the incident photons.

X-ray diffraction (XRD). The XRD patterns were collected by using a PANalytical X'Pert Pro X-ray powder diffractometer with Cu Kα radiation (λ = 1.54050 Å).

Temperature dependent electron mobility measurements. A Cryo Industries Liquid Nitrogen Dewars with Lake Shore model 335 cryogenic temperature controller was used to modulate the operating temperature of devices. We waited for 5 min after the temperature of system reached the target value, to ensure the device temperature stabilized. The cooling and heating rates were set as ~5 and ~2 K min^{-1}, respectively. Electron mobilities were obtained by using Keithley 2400 source-measure unit under dark. The *J*-*V* curves were fitted through using space-charge limited current (SCLC) method[S7] with a device structure of ITO/ZnO/ETL/BCP/Ag. The *J*-*V* curves of the devices were plotted as $\ln(Jd^3/V^2)$ vs. $(V/d)^{0.5}$ employing the following equation: $\ln(Jd^3/V^2) \cong 0.89(1/E_0)^{0.5} (V/d) + \ln(9\varepsilon_0\varepsilon_r\mu_e/8)$, and $V = V_{appl} - V_{bi}$, where J is the current density, d is the thickness of ETL, μ_e is the electron mobility, ε_r is the relative dielectric constant of the ETL, ε_0 is the permittivity of free space (8.85×10^{-12} F m^{-1}), V_{appl} is the voltage applied to the device, and V_{bi} is the built-in voltage due to the difference in work function of the two electrodes (for electron-only diodes, V_{bi} is 0 V).

Conductivity measurements. The tests were conducted by using Keithley 2400 source-measure unit in ambient atmosphere. The device structure was ITO/ETL/Ag. Resistance (R) of devices consists of resistance of ETL film (R_f) and contact resistance (R_c) between ETL and metal. The physical quantities in Figure S24c were derived from Figure S24b and the following equations: $R = R_c + R_f$, $I = \sigma AV/d$, $\sigma = d/RA$, where d is the thickness of fullerene derivative film, A is the device area.

Current density–voltage (*J*-*V*) measurements. The *J*-*V* characteristics of devices were obtained by using Keithley 2400 source-measure unit under AM 1.5G

illumination at 100 mW cm^{-2} with a Newport Thermal Oriel 91192 1000 W solar simulator in ambient atmosphere, and the light intensity was calibrated by a KG-5 Si cell in advance. The scan step was set as 0.02 V with different scan directions (forward scan: -0.2 to 1.2 V; reverse scan: 1.2 to -0.2 V; delay time: 0.3 s). The shading mask, which was used for *J-V* measurements, was certified as 0.08313 cm^2 at the National Institute of Metrology (NIM, China).

External quantum efficiency (EQE) measurements. The EQE spectrum was measured using Solar Cell Spectral Response Measurement System (Enlitech, QE-R3011). The light intensity at each wavelength was calibrated using a standard single crystal Si photovoltaic cell.

Photoluminescence/time-resolved photoluminescence (PL/TRPL) measurements. Steady-state PL and TRPL spectra were carried out on FLS980 (Edinburgh Instruments Ltd.) with an excitation at 470 nm. The samples were deposited on quartz substrates.

Electroluminescence (EL) measurements. The EL measurements were conducted by employing PSC devices as LEDs, and the LED devices were placed in an integrating sphere of the instrument (Enlitech, LQ-100X). The power output was collected for calculating the EQE of EL.

Ideal factor measurements. The light intensity dependence of V_{OC} for PSCs was measured by using Keithley 2420 source-measure unit under different illumination intensity with a solar simulator (SS-F5-3A, Enlitech) in nitrogen atmosphere.

Trap density (N_{trap}) calculation. *J-V* characteristics in dark were collected for electron-only devices with a structure of ITO/SnO_2/perovskite/bilayer ETL/Ag by Keithley 2400 source-measure unit. The N_{trap} was calculated by the equation: $N_{trap} = 2\varepsilon\varepsilon_0 V_{TFL}/eL^2$,[S8] where ε and ε_0 are the dielectric constants of perovskite and vacuum permittivity, respectively, V_{TFL} is trap-filled limit voltage, e is the elementary charge, L is the thickness of the perovskite film.

Film thickness measurements. The thickness of thin films was measured on a Bruker DektakXT profilometer.

Theory Calculation

Calculation of adsorption energy. We theoretically investigate the interaction between FP-C8 molecule and perovskite with/without Pb^{2+} defects by using density functional theory as implemented in the Vienna Ab initio Simulation Package (VASP).[S9] We use the Perdew-Burke-Ernzerhof (PBE) functional[S10] for treating the exchange-correlation between electrons. The projector augmented wave (PAW) pseudopotential[S11] is used to describe the interaction between valence electrons and ionic cores. The (001) surface of perovskite is used for the adsorption of FP-C8 molecules, while a supercell of 3×3×1 unit cells is used to avoid the influence of the periodic boundary condition. The 3×3×1 Monkhorst-Pack *k*-mesh is used to sample the first Brillouin zone.[S12] For geometry optimization, the cutoff energy for the plane-wave basis set is set to 520 eV, and the convergence thresholds for the total energy and atomic force components are set as 10^{-4} eV and 0.5 eV $Å^{-1}$, respectively.

The DFT-D2 correction method[S13] is applied to deal with the long-rang van der Waals interactions.

The adsorption energies (E_{ads}) of FP-C8 molecule on perovskite with/without Pb^{2+} defects are calculated by using the following equation: $E_{ads} = E$(FP-C8-adsorbed perovskite) - E(FP-C8) - E(perovskite), where E(FP-C8-adsorbed perovskite), E(FP-C8), and E(perovskite) represent the total energies of FP-C8-adsorbed perovskite, FP-C8 molecule, and perovskite, respectively. The optimized structures of FP-C8-adsorbed perovskite are plotted in Figure S20, and the corresponding chemical adsorption energies are -0.79 eV and -0.33 eV for structures with and without under-coordinated Pb^{2+} defects, respectively. The result manifests that the bond strength between FP-C8 molecule and Pb^{2+} is larger than that between FP-C8 molecules and I^- due to the Coulomb attraction between the electronegative FP-C8 and electropositive Pb^{2+}.

Calculation of molecular dipole moment. The dipole moment of FP-Cn derivatives was calculated using Materials Studio with classical simulation method. In this method, a forcefield is used to describe the potential energy surface of entire classes of molecules.[S14] Here universal forcefield was chosen, because it was parameterized for the full periodic table and has been carefully validated for organic molecules.[S15,S16] Charge equilibration (QEq) method was used for charge calculations.[S17] Conformational optimization was firstly performed depending on the selected forcefield. The conformations of FP-Cn derivatives were adjusted until the total energy of the structure was minimized (Figures S23a, c, e). Then, a detailed

modification was carried out with higher accuracy. The torsion angle of the C-O-C-C bond connecting the spacer and the terpyridine segment (yellow dash line in Figure S23) was considered as an important parameter involving the dipole moment. In this case, the total energy and dipole moment of FP-Cn derivatives were calculated with different torsion angles (Figures S23b, d, f).

Supporting Text

Text S1: Electron transport properties of FP-Cn derivatives. We fabricated space-charge limited electron-only devices with a structure of ITO/ZnO/ETL/BCP/Ag, and investigated their temperature dependent electron mobility (μ_e). As shown in Figure S25, the mobility of FP-C4 based device decreases from 2.1 $\times 10^{-4}$ cm^2 V^{-1} s^{-1} to 3.8 $\times 10^{-7}$ cm^2 V^{-1} s^{-1} (~ 553 times) with the device temperature cooling from 273 K to 123 K, while μ_e of FP-C12 based device decreases from 2.3 $\times 10^{-3}$ cm^2 V^{-1} s^{-1} to 2.1 $\times 10^{-4}$ cm^2 V^{-1} s^{-1} (~ 11 times). The energy disorder factor σ_1 of FP-C4 film is 0.029 eV, which is much larger than that of FP-C12 (0.018 eV) or FP-C8 (0.016 eV). Moreover, μ_e of the FP-C12 film at room temperature is 2.6 $\times 10^{-3}$ cm^2 V^{-1} s^{-1}, which is 7.6 times of that of the FP-C4 film (3.4 $\times 10^{-4}$ cm^2 V^{-1} s^{-1}), but smaller than FP-C8 (4.9 $\times 10^{-3}$ cm^2 V^{-1} s^{-1}) (Figure S26). These results reveal that FP-C8 exhibits a better charge transport property than FP-C4 and FP-C12 because of excellent solubility, relatively larger dipole moment (Figure S23) and stronger intermolecular stacking of FP-C8.

Text S2: Charge extraction ability of FP-Cn derivatives. The steady-state

photoluminescence (PL) and time-resolved photoluminescence (TRPL) decay were used to investigate the charge extraction ability of different FP-Cn derivatives. As shown in Figure S41a, compared with FP-C12, FP-C8 quenches PL more efficiently, and FP-C4 exhibits a worst quenching effect. Furthermore, perovskite film with FP-C12 ETL shows an average decay time (τ_{avg}) of 54.17 ns with an A_1 value of 46.32%, which is longer than that of FP-C8 (24.84 ns, A_1 = 53.41%) (Figures 5b and S41b, Table S6). These results suggest that FP-C8 possesses superior electron extraction ability than FP-C12, due to not only better alignment of LUMO energy levels, but also extended band bending on the interface caused by relatively larger dipole moment of FP-C8 (Figure S23). Perovskite film with FP-C4 ETL shows a longest τ_{avg} of 100.65 ns with an A_1 value of 9.45% (Figure S41b, Table S6), indicating that FP-C4 possesses inferior electron extraction ability, related to the limited solubility and film quality of FP-C4.

Text S3: Chelation/passivation effect of FP-Cn derivatives. We conducted electroluminescence (EL) measurements to probe the chelation/passivation effect of FP-Cn (Figures 5c-d and S42). The EL EQE of PSCs with FP-C4, FP-C8 and FP-C12 are 0.11%, 1.37% and 0.84%, respectively. The ideal factors of PSCs with FP-C4, FP-C8 and FP-C12 are 2.04, 1.47 and 1.61, respectively (Figure S43). These results reveal that the non-radiative recombination is more efficiently suppressed in FP-C8 based device than the others. Moreover, the trap concentration (N_{trap}) of FP-C4, FP-C8 and FP-C12 based electron-only devices is 9.9×10^{15} cm^{-3}, 1.9×10^{15} cm^{-3} and 2.9×10^{15} cm^{-3}, respectively (Figure S44). From these results we can conclude that FP-C8

possesses a better chelation and passivation ability than FP-C4 and FP-C12 owing to suitable linker length, which ensures good solubility and film-forming ability as well as relatively larger dipole moment.

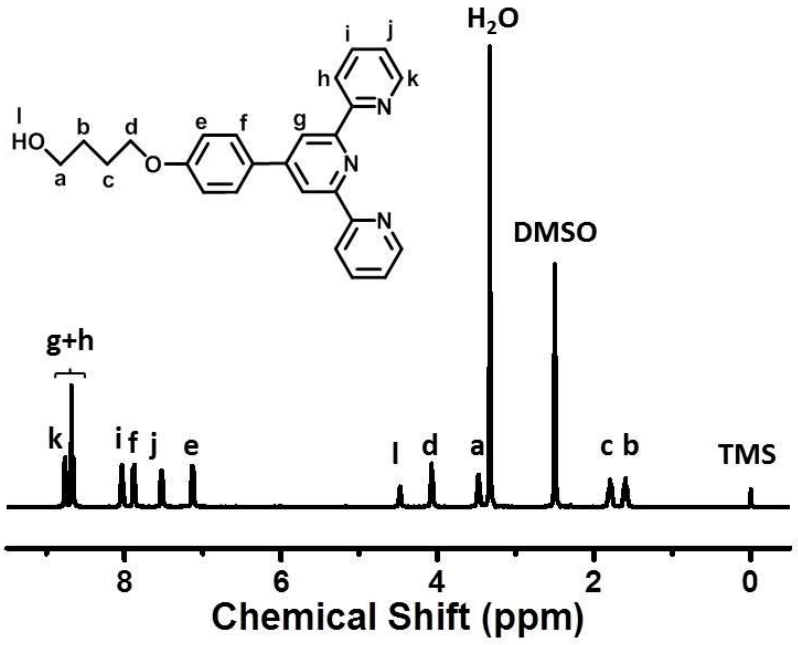

Figure S1. ^{1}H NMR spectrum of P-C4.

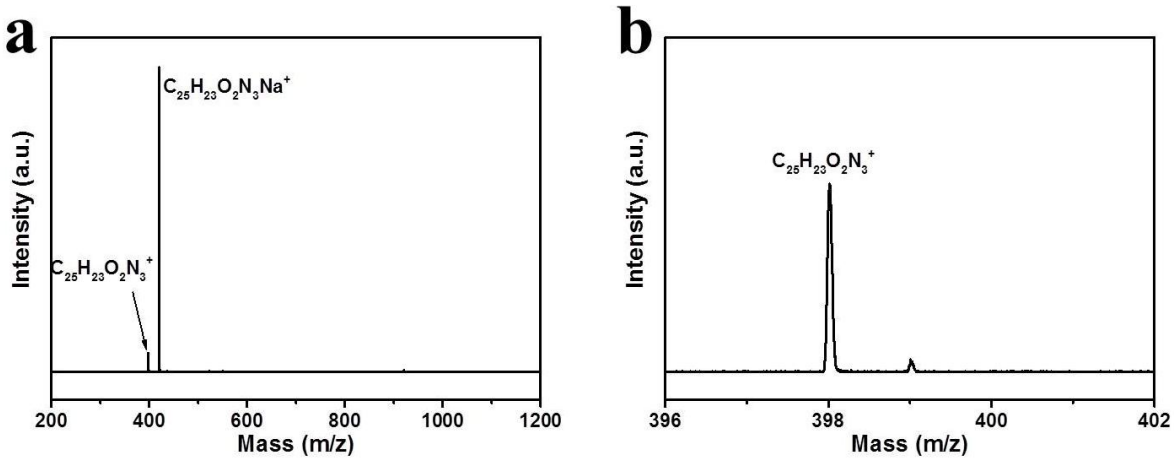

Figure S2. (a, b) MALDI-TOF mass spectra of P-C4: The overview of the spectrum (a); The zoom-in view of the spectrum (b).

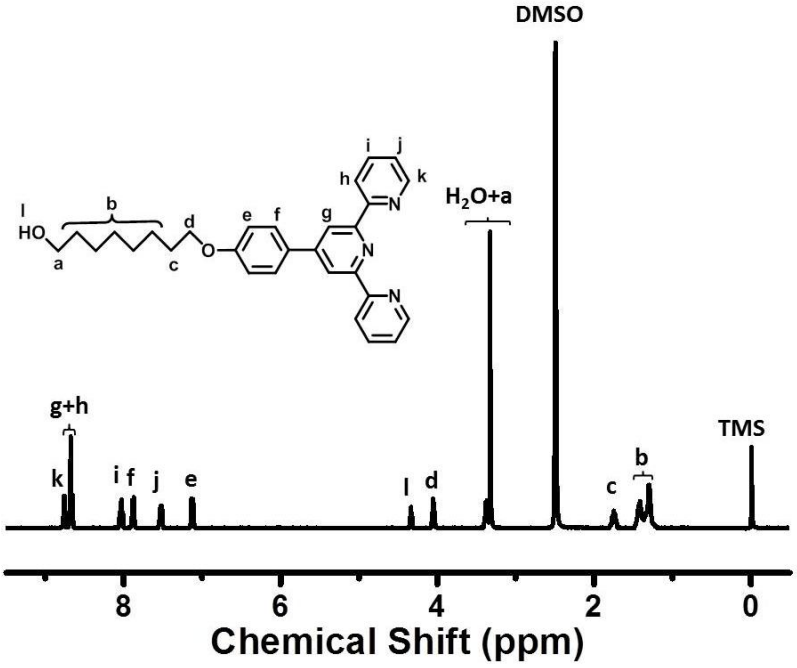

Figure S3. ^{1}H NMR spectrum of P-C8.

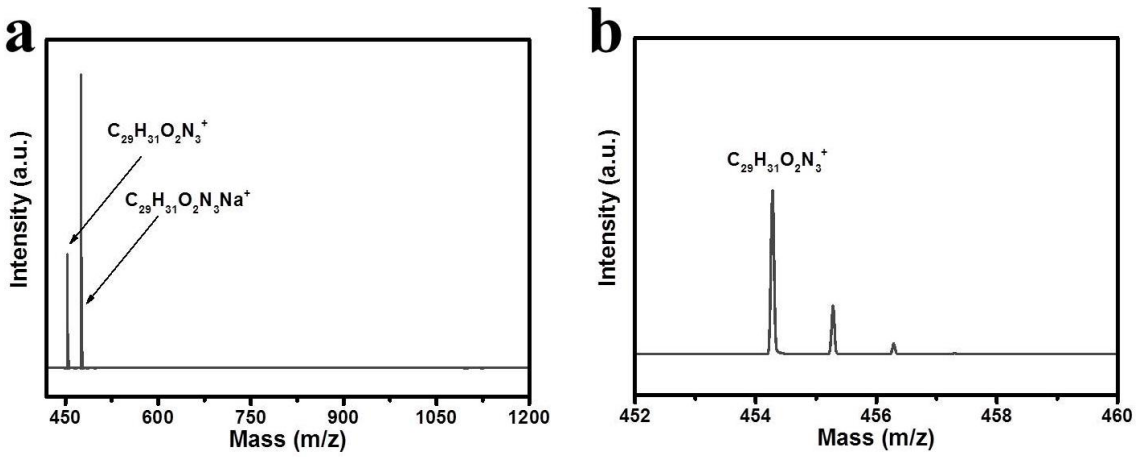

Figure S4. (a, b) MALDI-TOF mass spectra of P-C8: The overview of the spectrum (a); The zoom-in view of the spectrum (b).

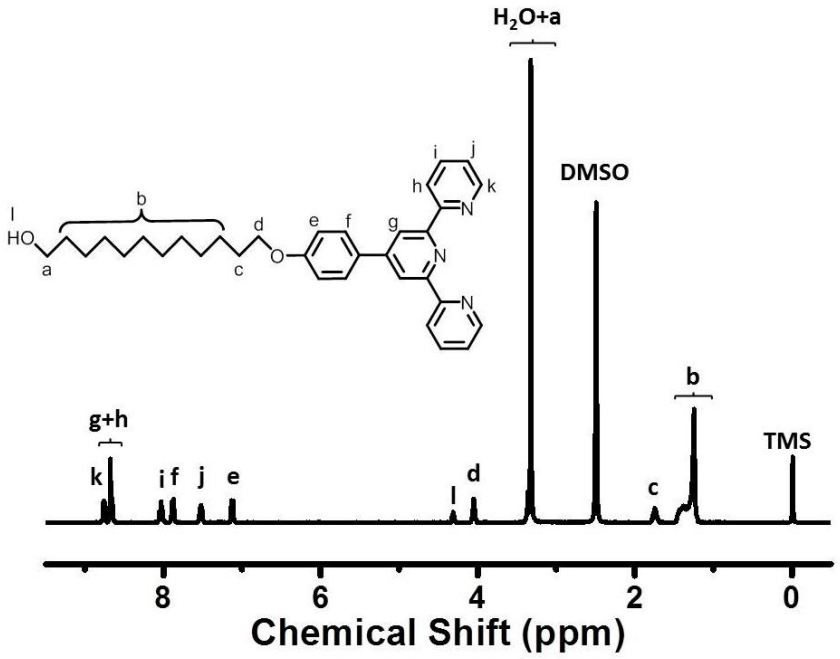

Figure S5. ^{1}H NMR spectrum of P-C12.

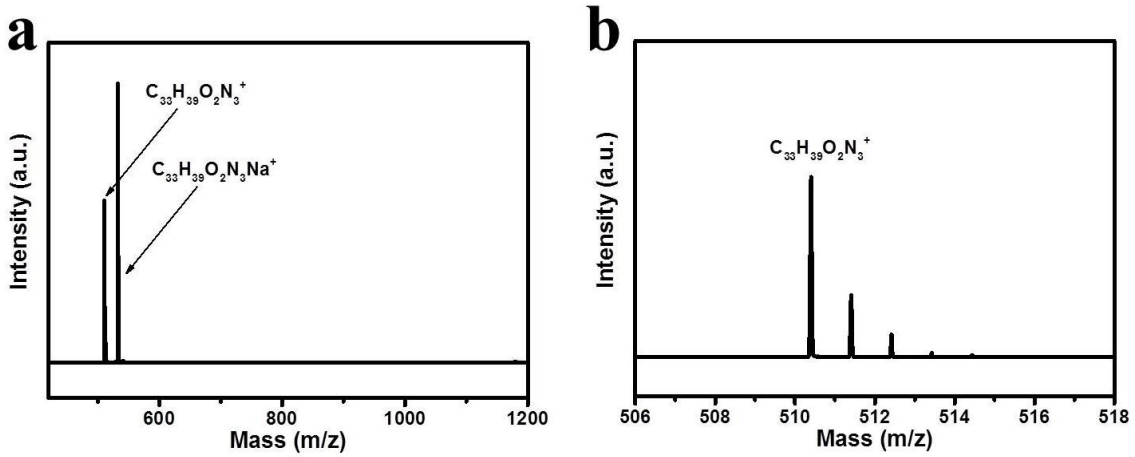

Figure S6. (a, b) MALDI-TOF mass spectra of P-C12: The overview of the spectrum (a); The zoom-in view of the spectrum (b).

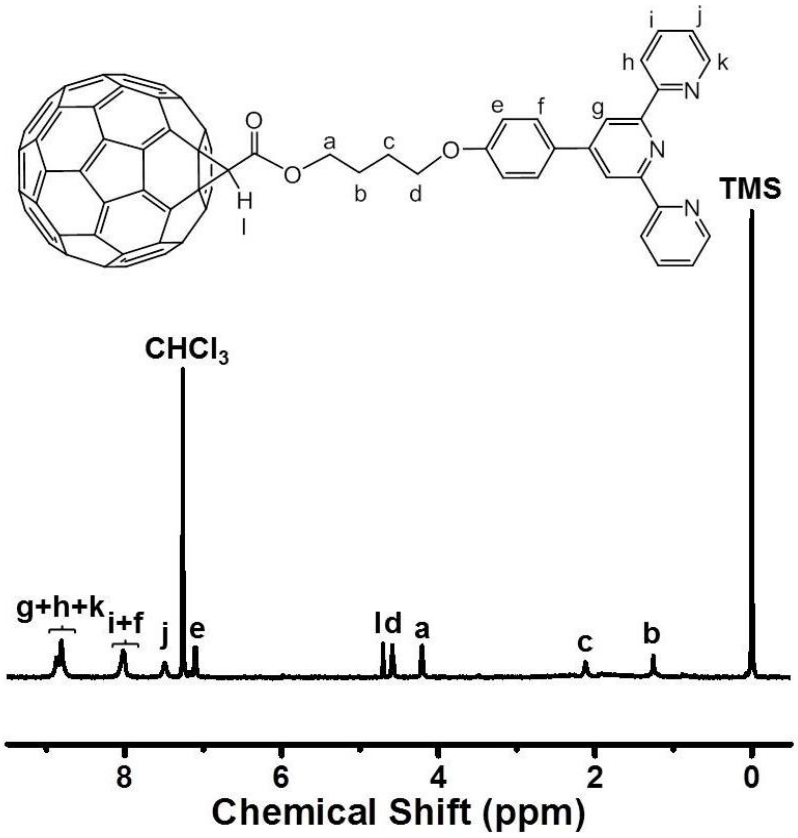

Figure S7. ^{1}H NMR spectrum of FP-C4.

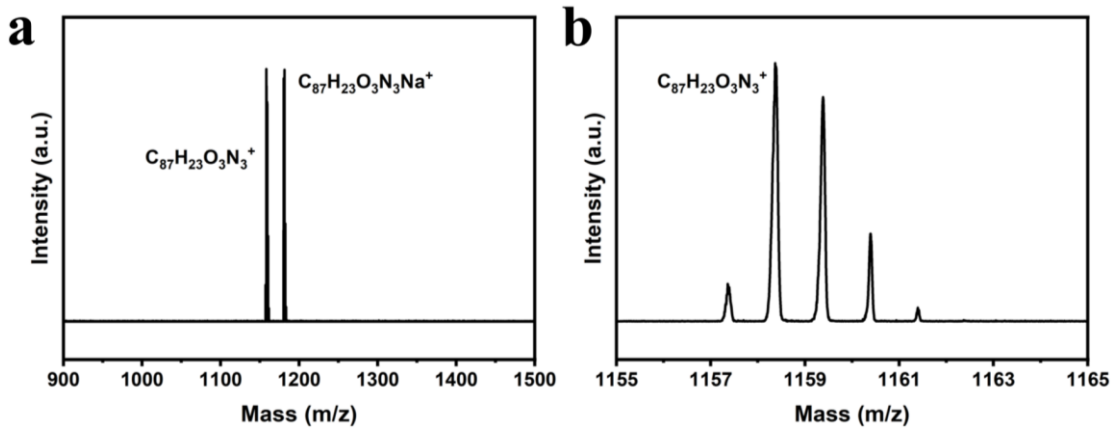

Figure S8. (a, b) MALDI-TOF mass spectra of FP-C4: The overview of the spectrum (a); The zoom-in view of the spectrum (b).

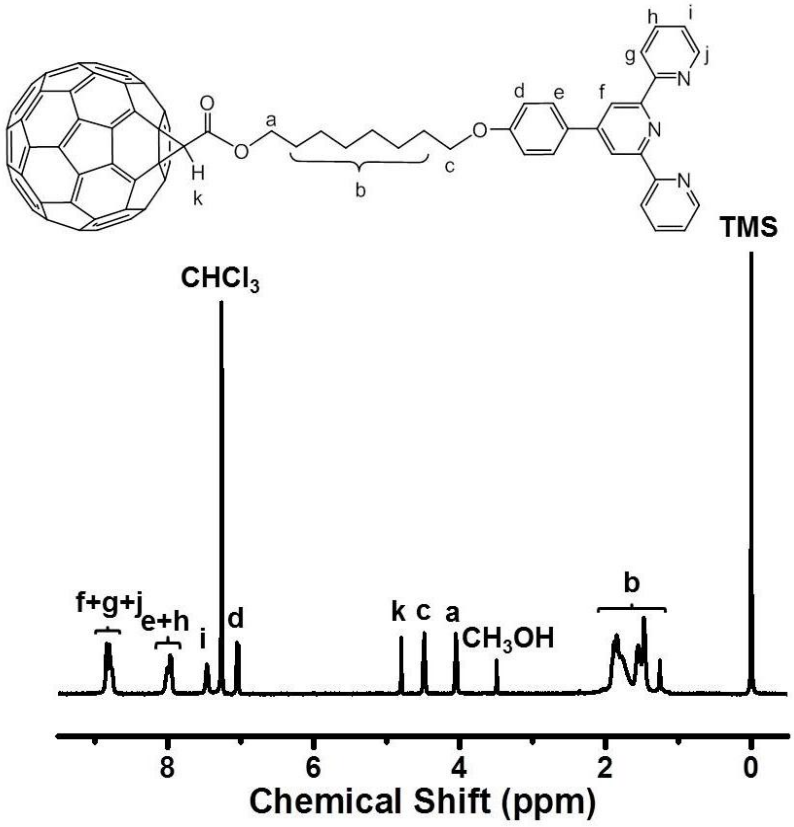

Figure S9. ^{1}H NMR spectrum of FP-C8.

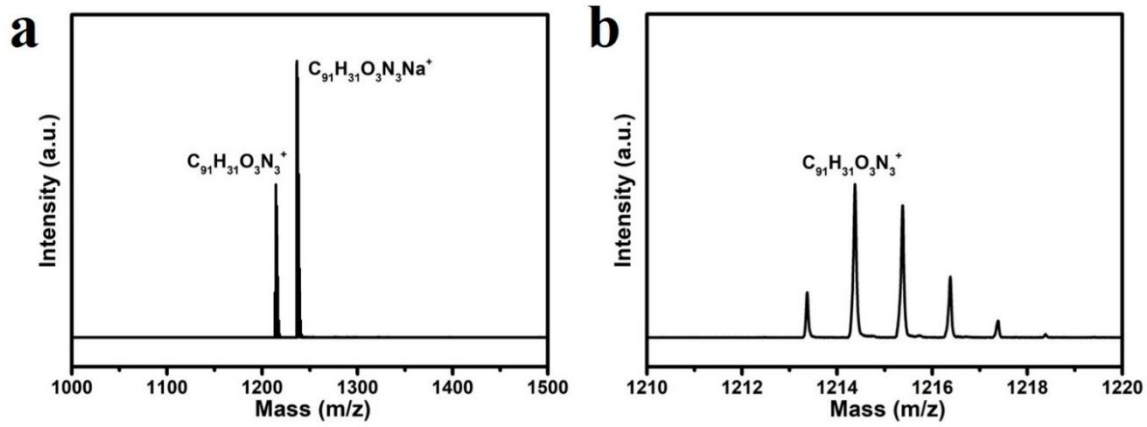

Figure S10. (a, b) MALDI-TOF mass spectra of FP-C8: The overview of the spectrum (a); The zoom-in view of the spectrum (b).

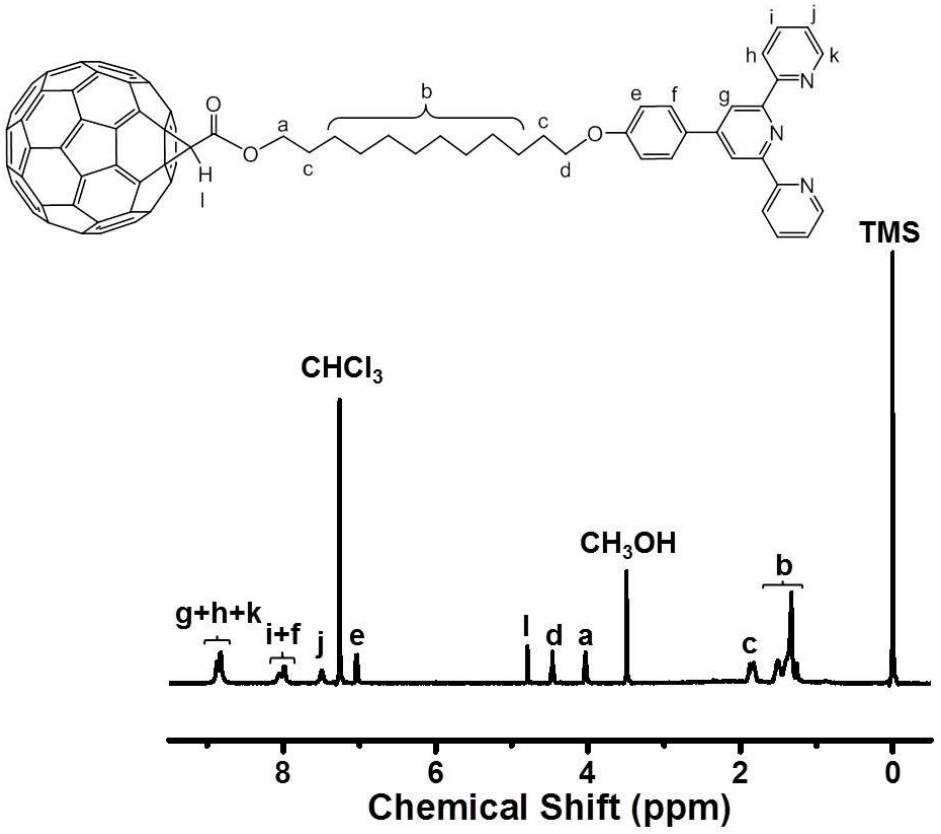

Figure S11. ^{1}H NMR spectrum of FP-C12.

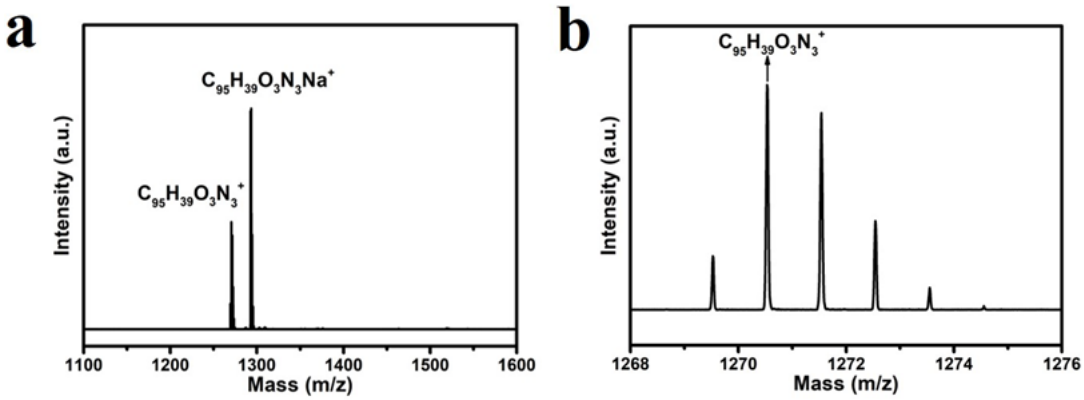

Figure S12. (a, b) MALDI-TOF mass spectra of FP-C12: The overview of the spectrum (a); The zoom-in view of the spectrum (b).

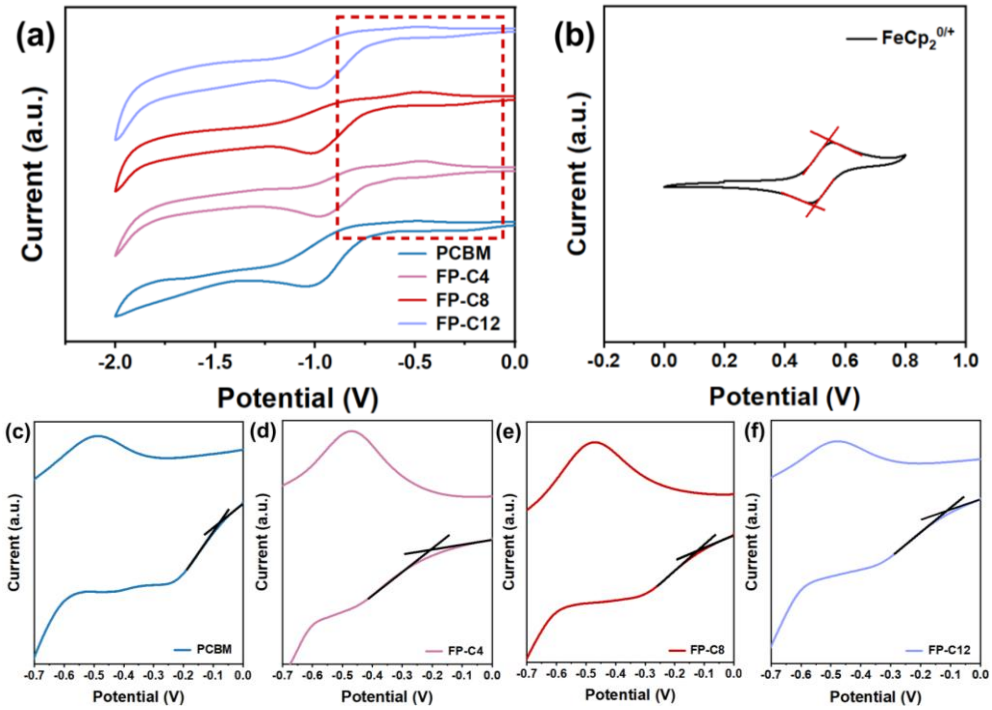

Figure S13. (a) Cyclic voltammograms for PCBM, FP-C4, FP-C8 and FP-C12 in CH_3CN/0.1 M $[Bu_4N]^+[PF_6]^-$ at 100 mV s^{-1}, in which the horizontal scale refers to an Ag/AgCl electrode as a reference electrode. (b) Cyclic voltammogram for reference ferrocene. (c-f) Partially enlarged views of cyclic voltammograms for PCBM (c), FP-C4 (d), FP-C8 (e) and FP-C12 (f), respectively.

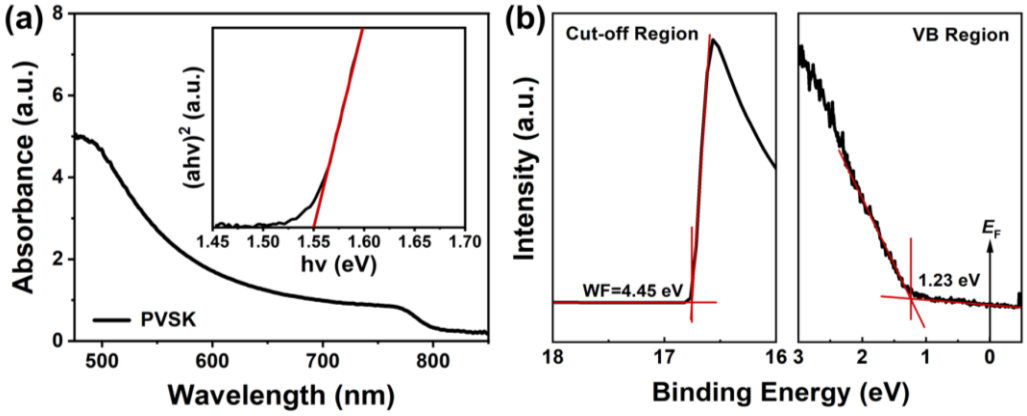

Figure S14. (a) UV-Vis spectra of pristine CsFAMA perovskite film, inset is the corresponding Tauc plot. (b) UPS data for pristine CsFAMA perovskite films. All the samples were prepared on ITO/PTAA/PFN-Br substrates.

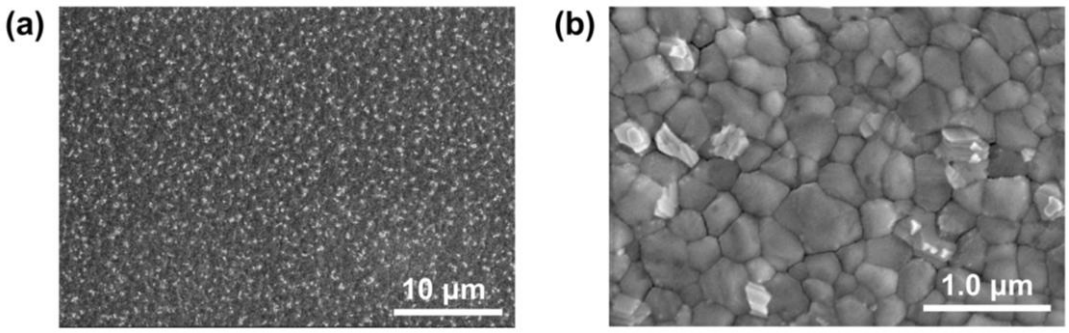

Figure S15. (a, b) SEM images of pristine CsFAMA perovskite films with different magnification: ×3.00K (a); ×35.0K (b).

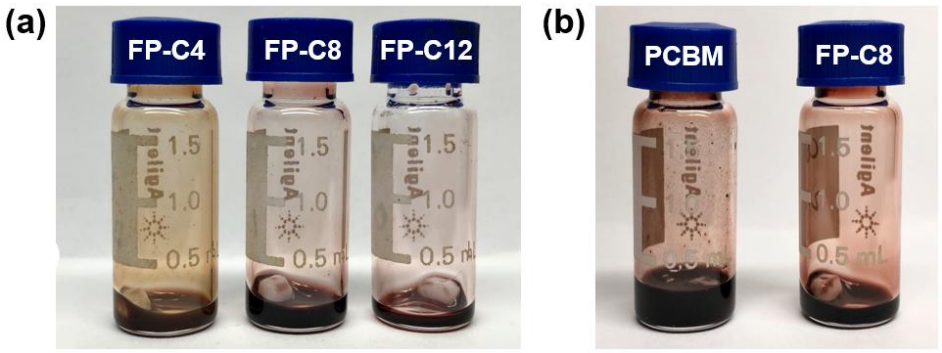

Figure S16. (a) Photographs of 20 mg mL^{-1} DCB solutions for FP-C4, FP-C8 and FP-C12. (b) Photographs of PCBM (50 mg mL^{-1} DCB) and FP-C8 (75 mg mL^{-1} DCB) concentrated solutions.

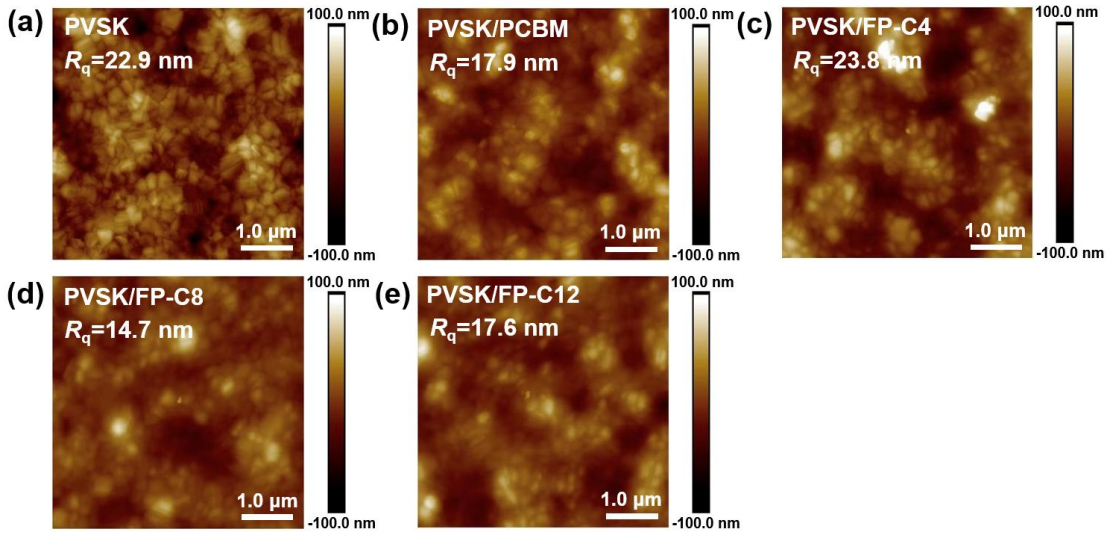

Figure S17. (a-e) AFM height images of pristine CsFAMA perovskite film (a) and perovskite coated with 30 nm films of PCBM (b), FP-C4 (c), FP-C8 (d) and FP-C12 (e).

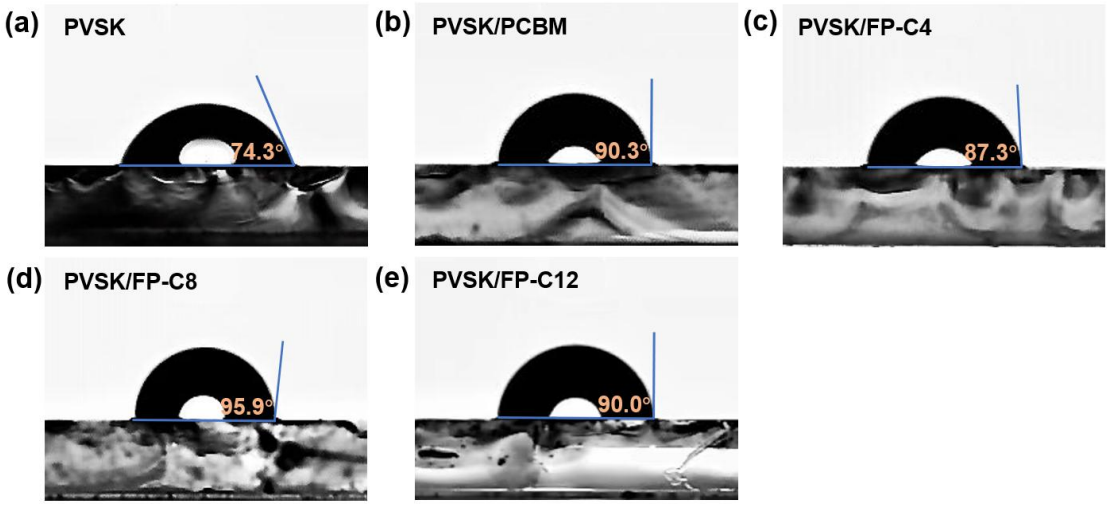

Figure S18. (a-e) Contact angle measurements with water droplet on top of pristine CsFAMA perovskite film (a) and perovskite coated with 30 nm films of PCBM (b), FP-C4 (c), FP-C8 (d) and FP-C12 (e).

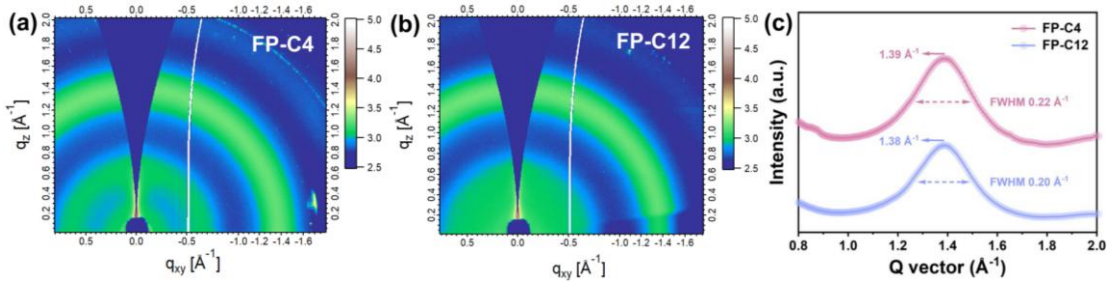

Figure S19. (a, b) GIWAXS patterns of 30 nm films of FP-C4 (a) and FP-C12 (b) prepared on Si wafers. (c) Line cut of π-π stacking peak of out-of-plane direction for FP-C4 and FP-C12 films.

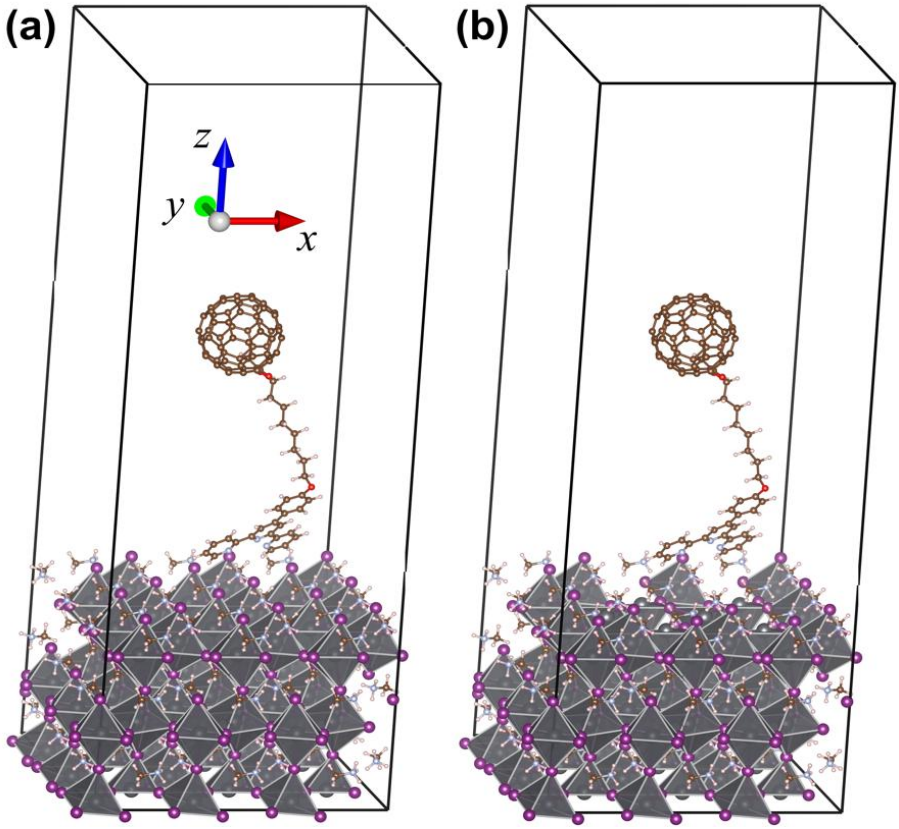

Figure S20. Optimized structures of FP-C8-adsorbed perovskite without defects (a) and with under-coordinated Pb^{2+} defects (b).

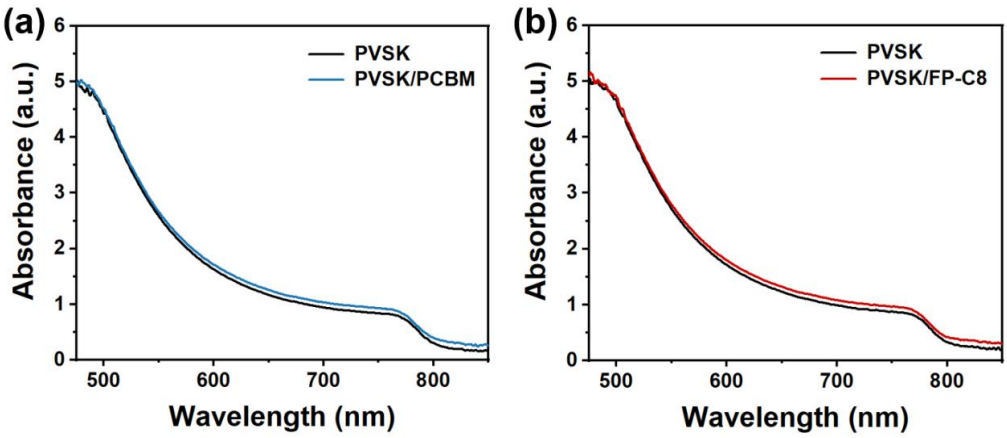

Figure S21. (a, b) UV-Vis spectra for pristine CsFAMA perovskite film and perovskite coated with 30 nm PCBM (a) or FP-C8 film (b).

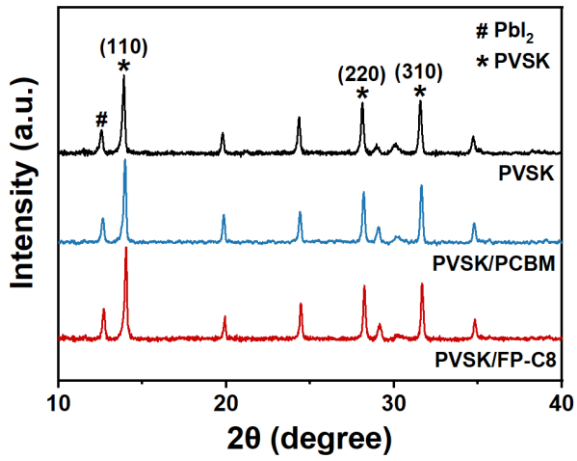

Figure S22. XRD spectra for pristine CsFAMA perovskite film and perovskite coated with 30 nm PCBM or FP-C8 film.

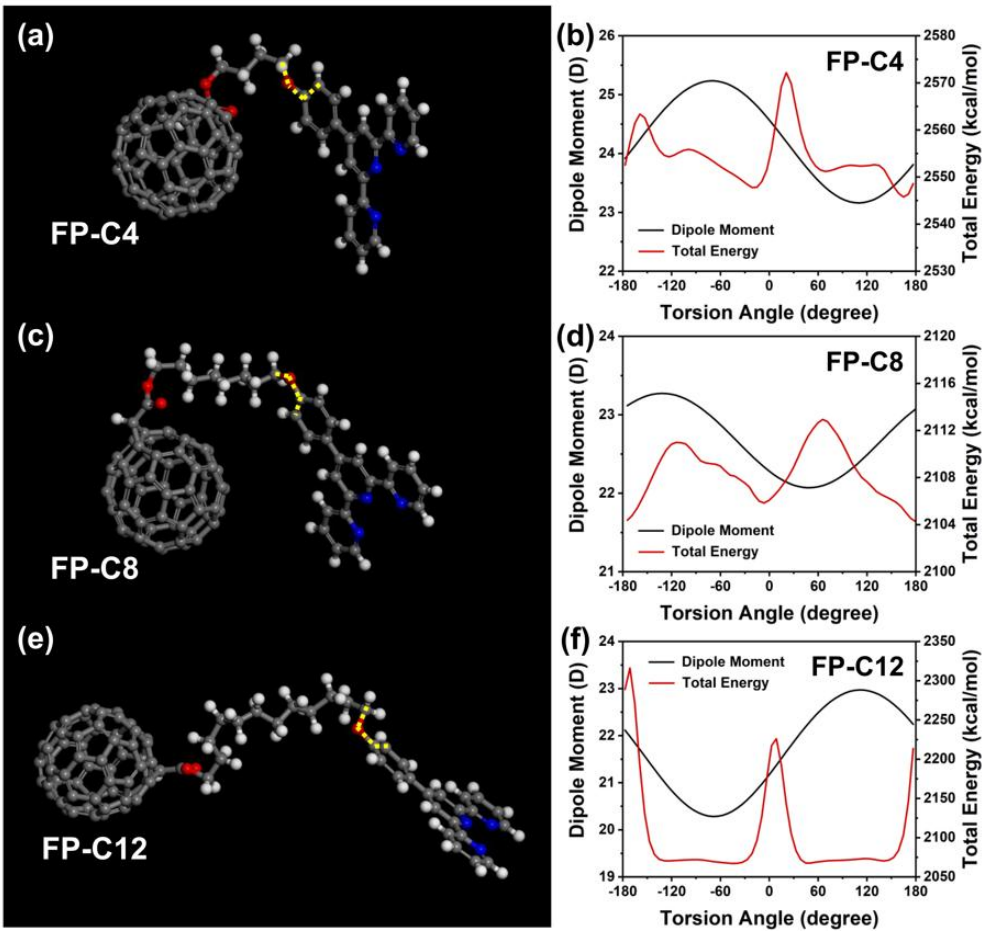

Figure S23. Molecular structures with lowest total energy of FP-C4 (a), FP-C8 (c) and FP-C12 (e); The changes of dipole moment and total energy with torsion angle of the C-O-C-C bond (yellow dash line in the model) for FP-C4 (b), FP-C8 (d) and FP-C12 (f).

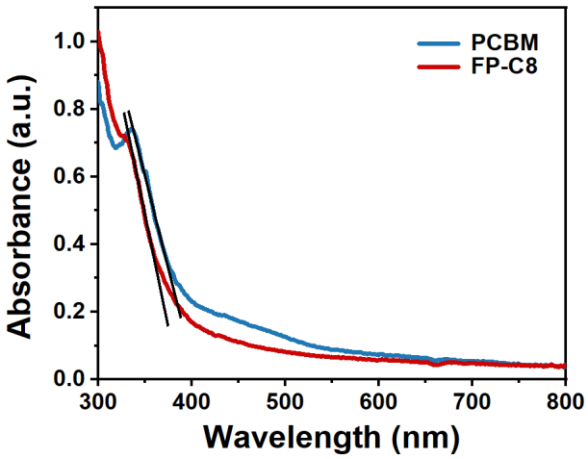

Figure S24. UV-Vis spectra for 80 nm PCBM and FP-C8 films on glass substrates.

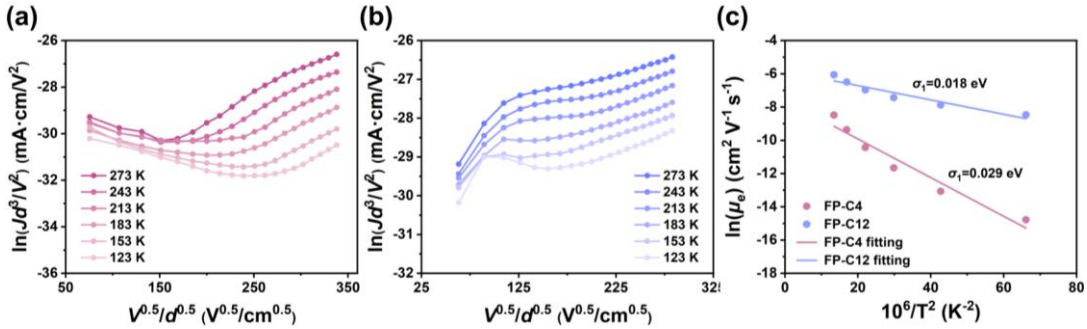

Figure S25. (a, b) Temperature dependence of electron transport for FP-C4 (a) and FP-C12 films (b). (c) Temperature dependence of electron mobility in FP-C4 and FP-C12 films in ln(μ_e) vs. T^{-2} representation.

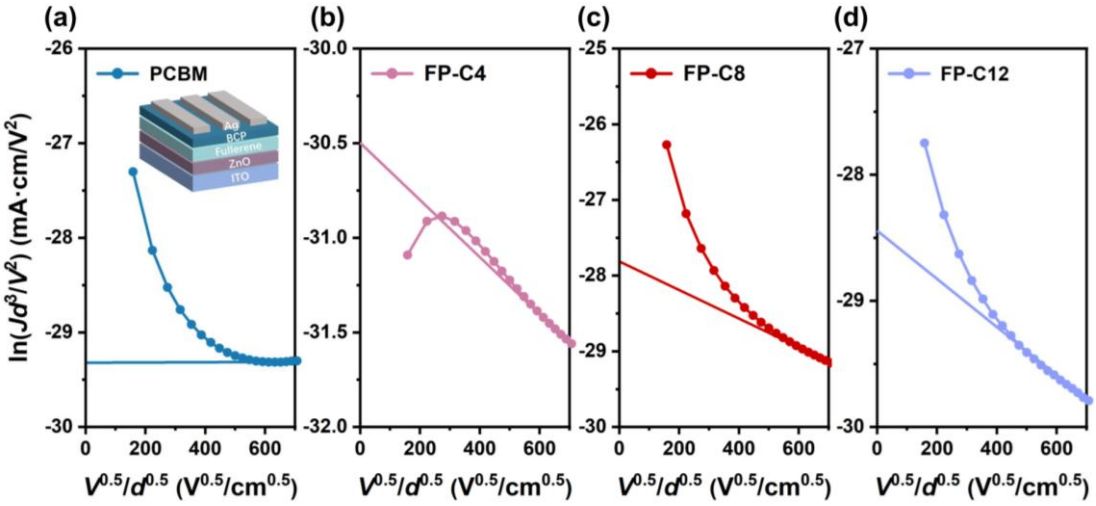

Figure S26. *J-V* characteristics in dark for electron-only devices based on different fullerene derivatives (Inset of (a) is the schematic illustration of device structure).

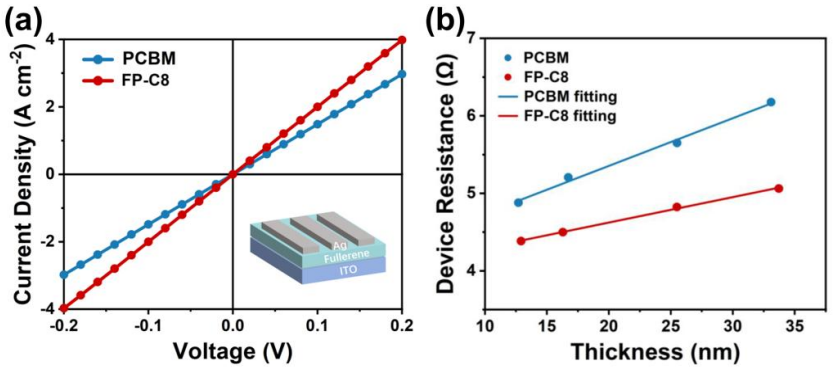

(c)

PCBM		FP-C8	
R (12.7 nm)	4.88 Ω	*R* (12.9 nm)	4.38 Ω
R (16.7 nm)	5.20 Ω	*R* (16.3 nm)	4.50 Ω
R (25.5 nm)	5.65 Ω	*R* (25.5 nm)	4.82 Ω
R (33.1 nm)	6.18 Ω	*R* (33.7 nm)	5.06 Ω
R_C	4.13 Ω	R_C	3.95 Ω
σ_c (mS cm^{-1})	1.4×10^{-3}	σ_c (mS cm^{-1})	2.6×10^{-3}

Figure S27. (a) Conductivity measurement for 30 nm PCBM or FP-C8 film (Inset is the schematic illustration of device structure). (b) Film thickness dependence of resistance in PCBM and FP-C8 based devices. (c) Conductivity (σ_c) of PCBM and FP-C8 films.

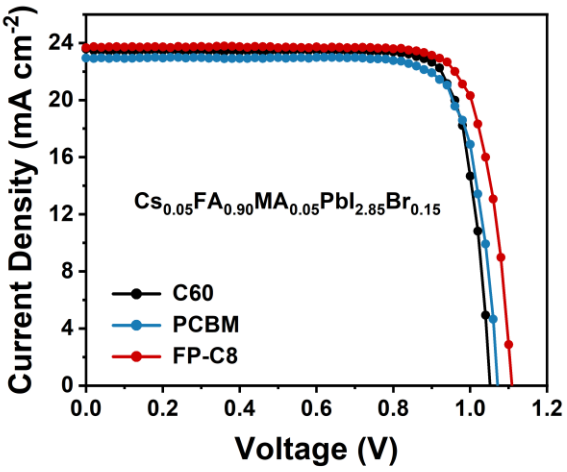

Figure S28. *J-V* curves of CsFAMA-based devices with C60, PCBM or FP-C8 single layer ETL.

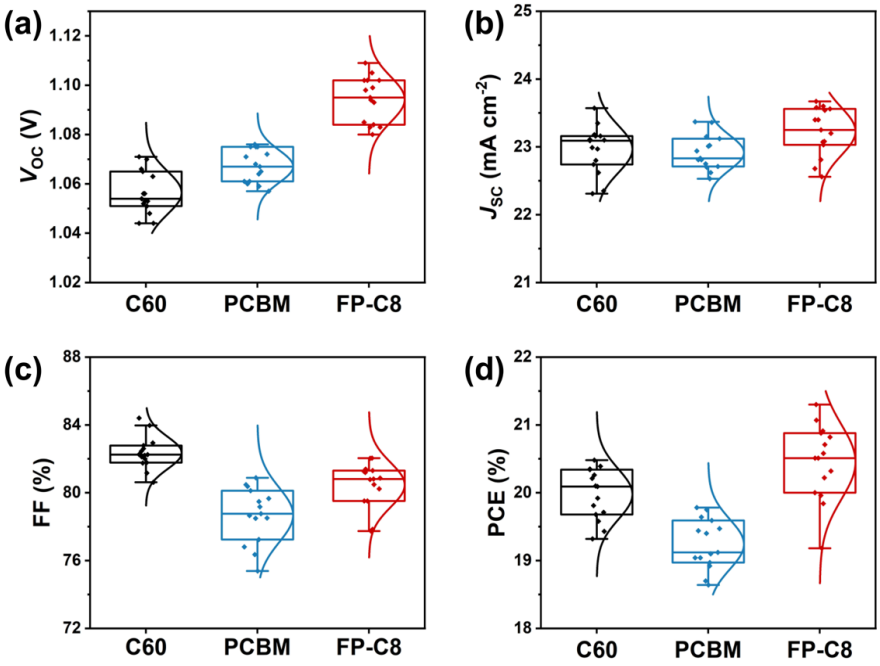

Figure S29. Statistics of V_{OC} (a), J_{SC} (b), FF (c) and PCE (d) distribution for CsFAMA-based PSCs with C60, PCBM or FP-C8 single layer ETL under AM 1.5G illumination (The data were collected from 15 devices).

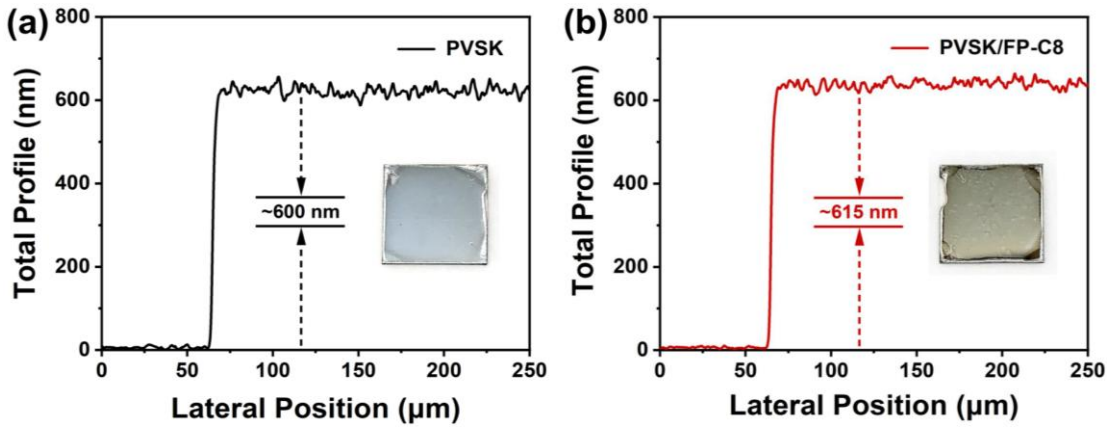

Figure S30. Thickness of (a) CsFAMA perovskite film and (b) CsFAMA perovskite film with FP-C8 ETL (20 mg mL^{-1} in DCB, 3000 rpm) obtained by DektakXT stylus profiler.

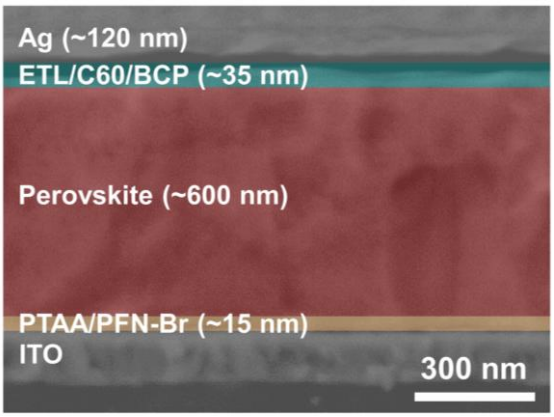

Figure S31. Cross-sectional SEM images of CsFAMA-based PSC device with bilayer ETL.

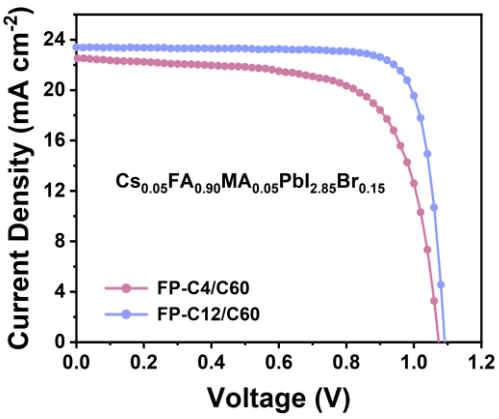

Figure S32. *J-V* curves of CsFAMA-based devices with FP-C4/C60 or FP-C12/C60 bilayer ETL under AM 1.5G illumination.

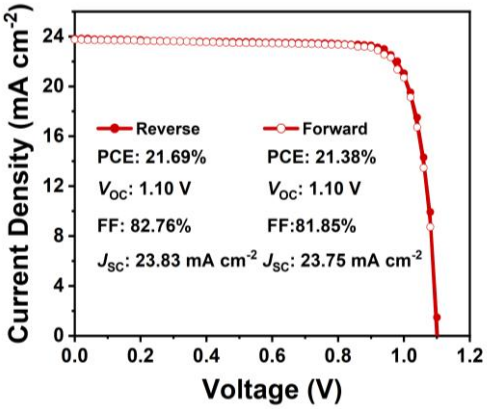

Figure S33. *J-V* curves of CsFAMA-based device with FP-C8/C60 bilayer ETL with different scan directions under AM 1.5G illumination.

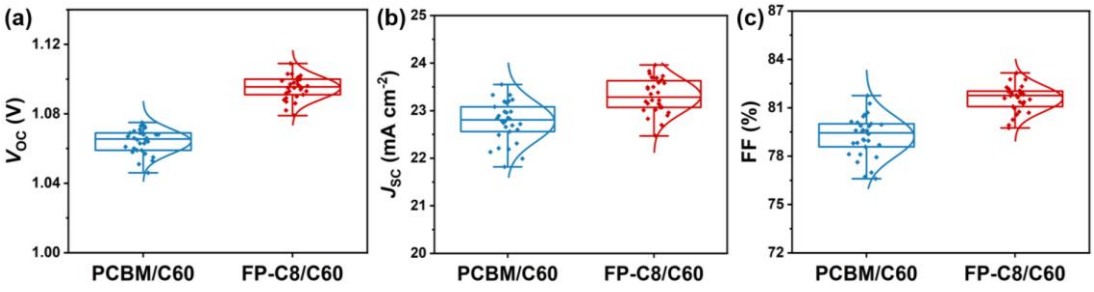

Figure S34. (a-c) Statistics of V_{OC} (a), J_{SC} (b), and FF (c) distribution for CsFAMA-based PSCs with PCBM/C60 or FP-C8/C60 bilayer ETL under AM 1.5G illumination (The data were collected from 30 devices).

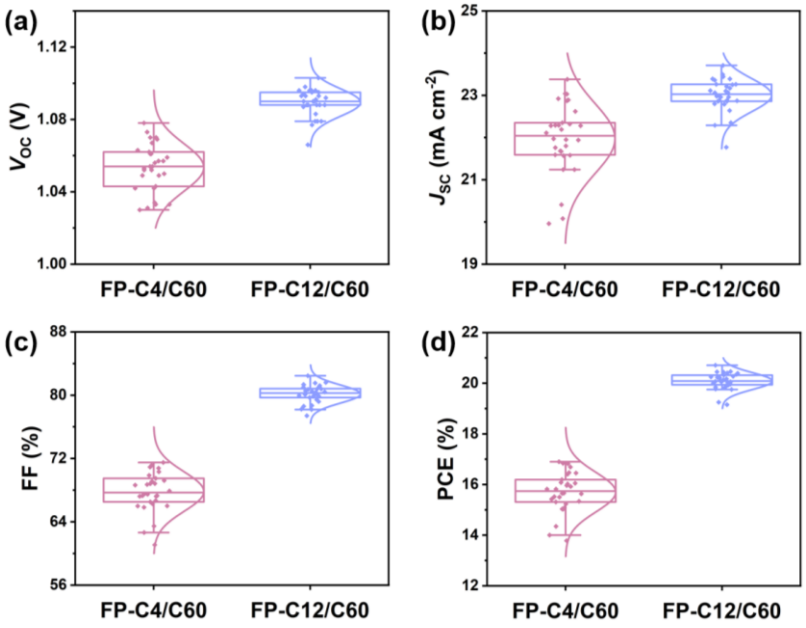

Figure S35. Statistics of V_{OC} (a), J_{SC} (b), FF (c) and PCE (d) distribution for CsFAMA-based PSCs with FP-C4/C60 or FP-C12/C60 bilayer ETL under AM 1.5G illumination (The data were collected from 30 devices).

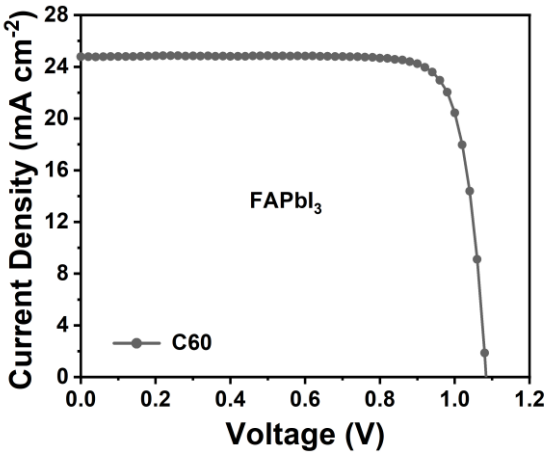

Figure S36. *J-V* curve of $FAPbI_3$ based device with C60 single layer ETL.

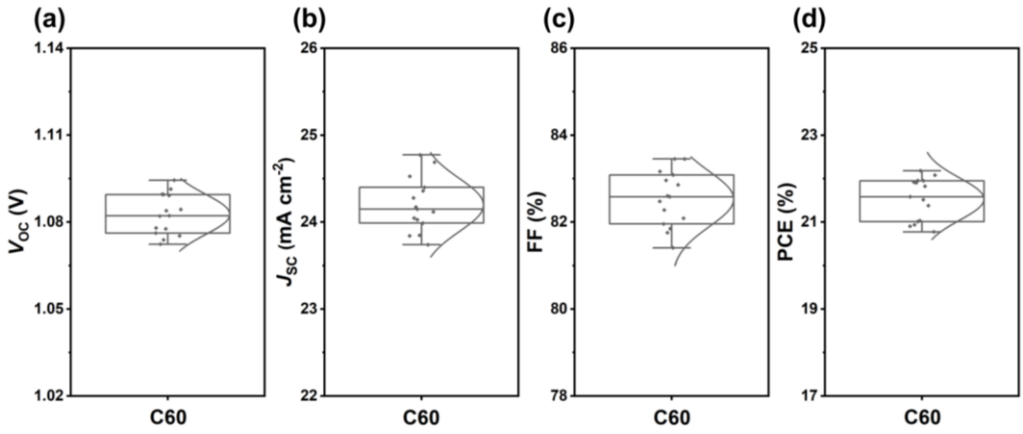

Figure S37. Statistics of V_{OC} (a), J_{SC} (b), FF (c) and PCE (d) distribution for $FAPbI_3$ based PSCs with C60 single layer ETL under AM 1.5G illumination (The data were collected from 15 devices).

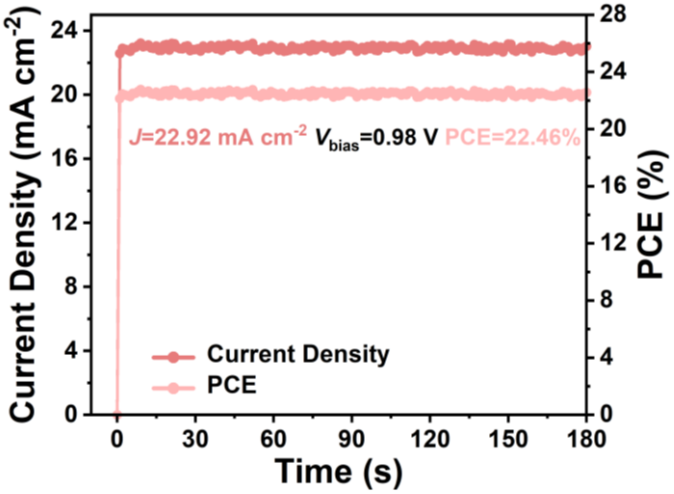

Figure S38. Steady-state photocurrent/power output of the $FAPbI_3$ based device with FP-C8/C60 bilayer ETL tracked at the maximum power point under AM 1.5G illumination.

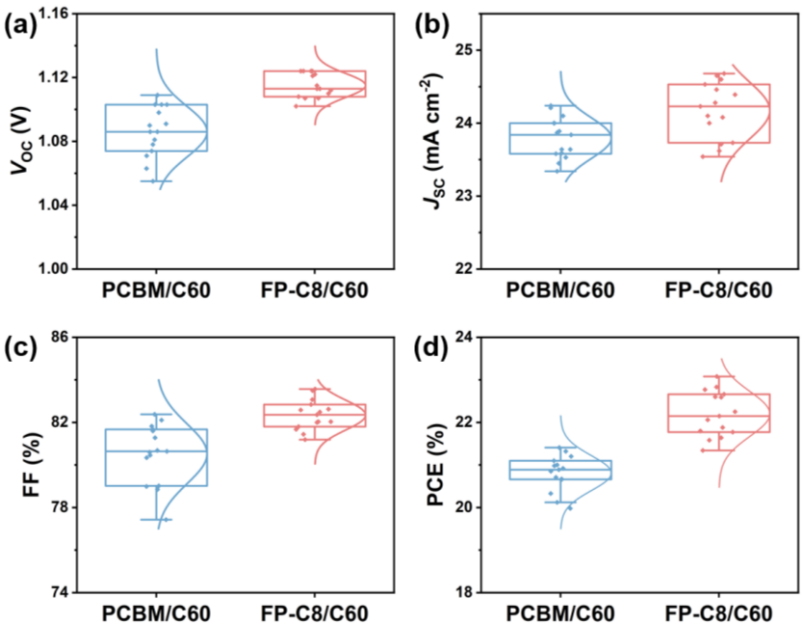

Figure S39. (a-d) Statistics of V_{OC} (a), J_{SC} (b), FF (c) and PCE (d) distribution for $FAPbI_3$ based PSCs with PCBM/C60 or FP-C8/C60 bilayer ETL under AM 1.5G illumination (The data were collected from 15 devices).

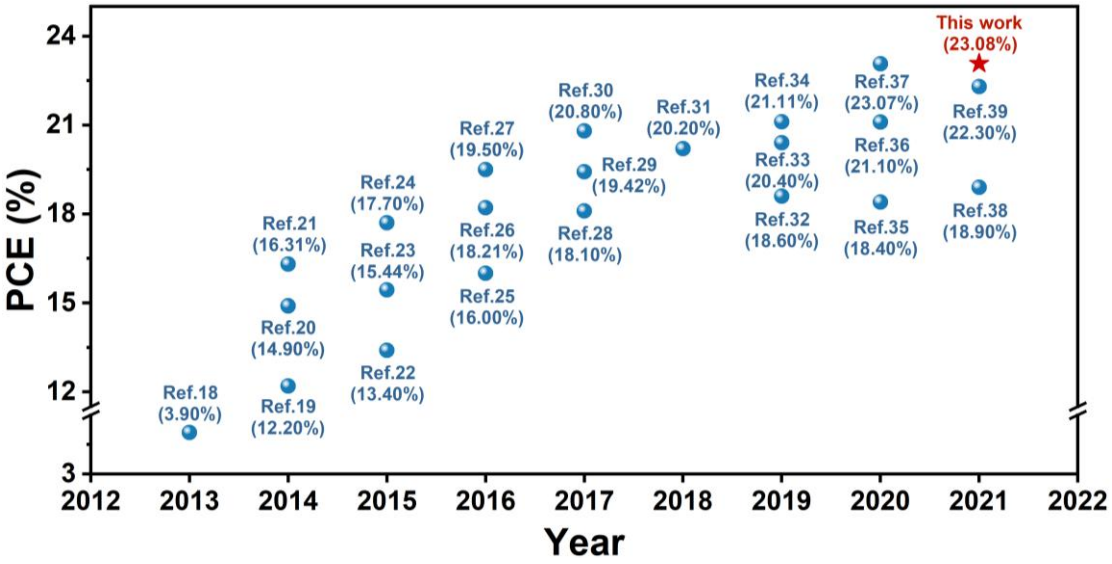

Figure S40. The summary of the state-of-the-art efficiencies for inverted planar PSCs with solution-processed fullerene derivatives.[S18-S39]

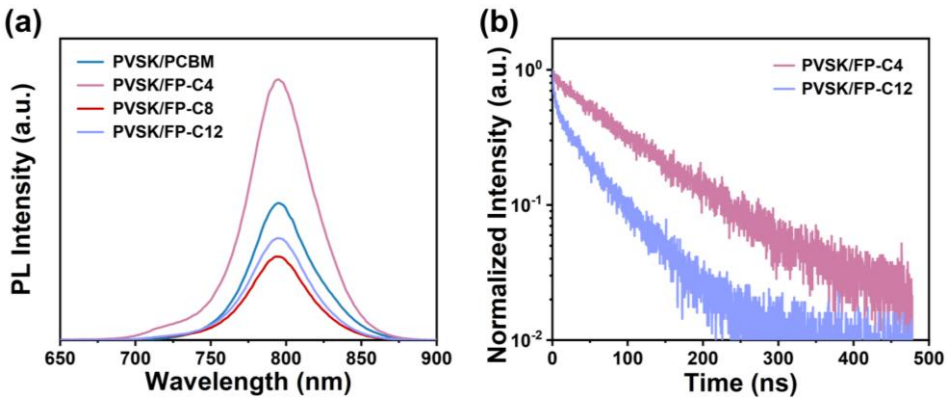

Figure S41. Steady-state PL spectra of CsFAMA perovskite with PCBM or FP-Cn single layer ETL (a) and TRPL decay transient spectra of CsFAMA perovskite with FP-C4 or FP-C12 single layer ETL on quartz substrate (b).

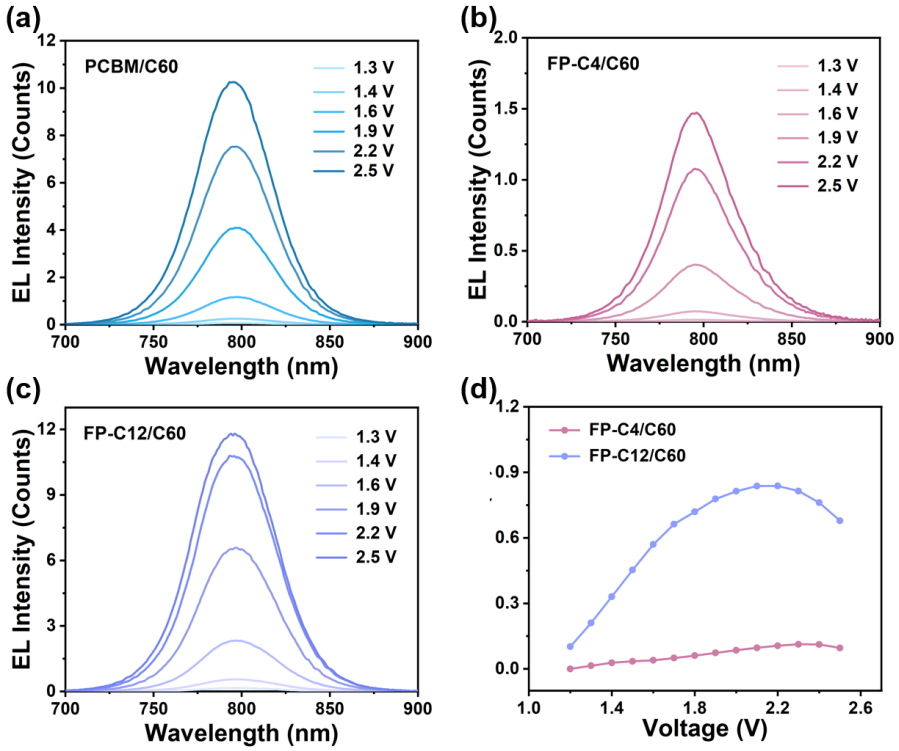

Figure S42. (a-c) EL spectra of the devices with PCBM/C60, FP-C4/C60 or FP-C12/C60 under different bias voltage while operating as LED. (d) EQE of EL of the devices with FP-C4/C60 or FP-C12/C60 while operating as LED.

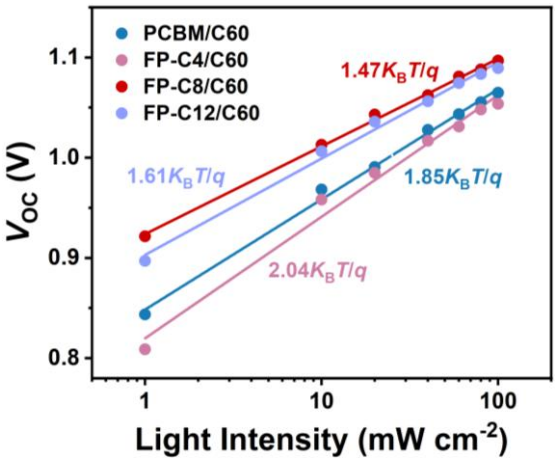

Figure S43. Light intensity dependence of V_{OC} for CsFAMA-based PSCs with different bilayer ETLs.

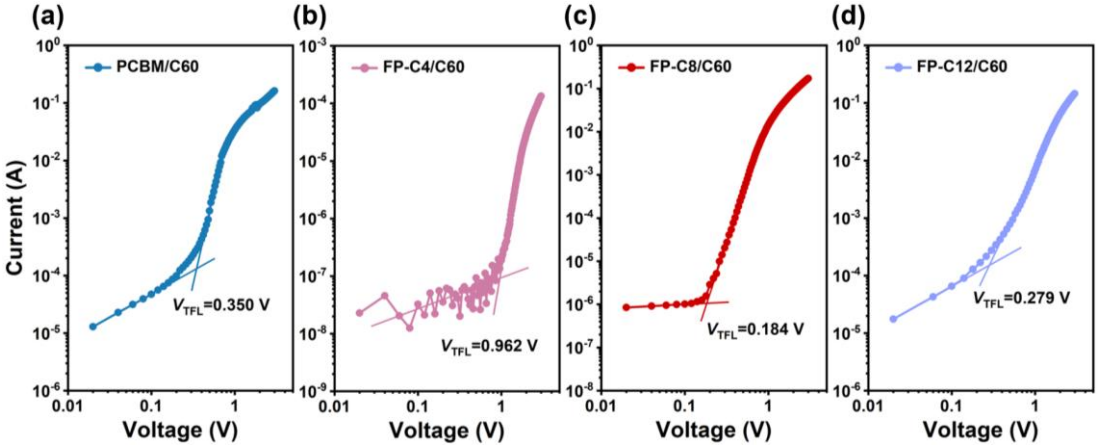

Figure S44. *J-V* characteristics in dark for electron-only devices (ITO/SnO_2/ CsFAMA perovskite/bilayer ETL/Ag).

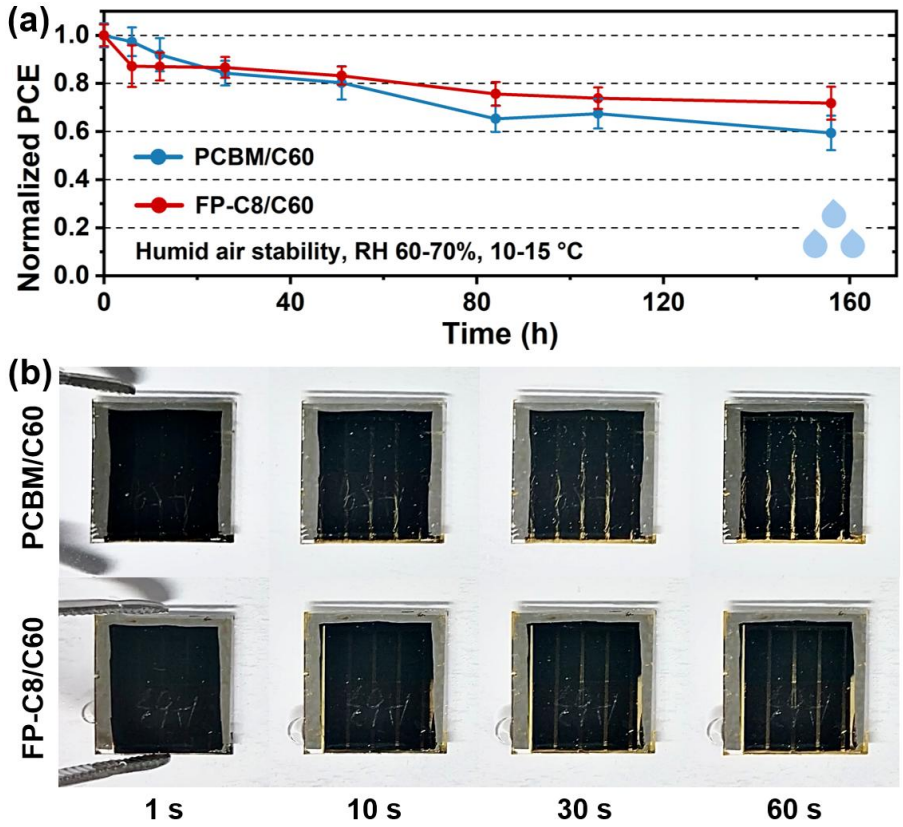

Figure S45. (a) Stability of the unencapsulated $FAPbI_3$ based PSCs with PCBM/C60 or FP-C8/C60 stored in dark and ambient atmosphere (relative humidity (RH) 60-70%, 10-15 ℃). (b) Color change of the unencapsulated $FAPbI_3$ based PSCs with PCBM/C60 or FP-C8/C60 immersing in water after different time.

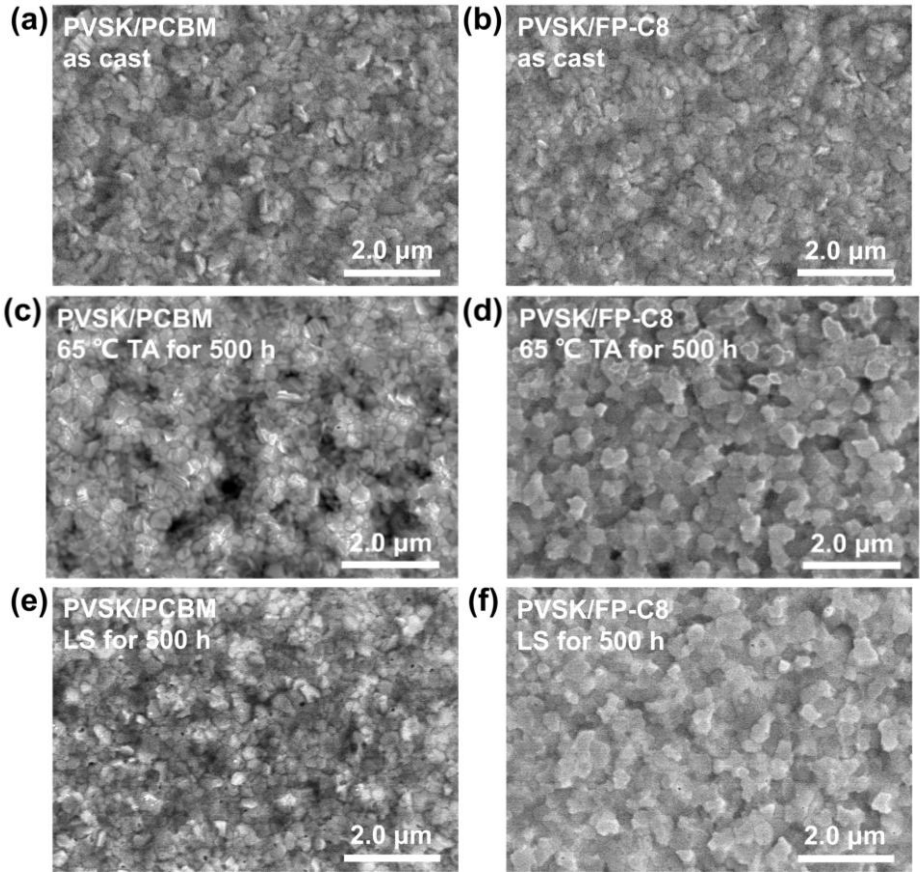

Figure S46. (a-f) SEM images of CsFAMA perovskite films with PCBM or FP-C8 under different conditions (with a magnification of ×15.00K): as cast (a, b); under dark and 65 ℃ continuous thermal annealing (TA) in N_2-filled glovebox for 500 hours (c, d); continuous light soaking (LS) with a white LED lamp (100 mW cm^{-2}) in N_2-filled glovebox for 500 hours (e, f).

Table S1. Parameters of different fullerene derivative films obtained from GIWAXS.

fullerene	FWHM ($Å^{-1}$)	CL (Å)	location ($Å^{-1}$)	*d*-spacing (Å)
PCBM	0.23	24.40	1.37	4.58
FP-C4	0.22	25.12	1.39	4.53
FP-C8	0.21	26.84	1.40	4.50
FP-C12	0.20	27.72	1.38	4.54

Table S2. Photovoltaic parameters of CsFAMA-based PSCs with C60, PCBM or FP-C8 single layer ETL under AM1.5G illumination[a].

ETL	V_{OC} (V)	J_{SC} (mA cm^{-2})	FF (%)	PCE (%)
C60	1.06 ±0.01	22.97 ±0.35	82.35 ±0.95	19.98 ±0.37
	(1.05)	(23.57)	(82.60)	(20.48)
PCBM	1.07 ±0.01	22.92 ±0.25	78.69 ±1.62	19.24 ±0.37
	(1.07)	(22.94)	(80.47)	(19.78)
FP-C8	1.09 ±0.01	23.23 ±0.35	80.46 ±1.32	20.45 ±0.55
	(1.11)	(23.67)	(81.20)	(21.30)

[a]Average values with standard deviation were obtained from 15 devices, the values in parentheses are the parameters of the best device.

Table S3. Photovoltaic parameters of CsFAMA-based PSCs with PCBM/C60 or FP-Cn/C60 bilayer ETL under AM1.5G illumination[a].

ETL	V_{OC} (V)	J_{SC} (mA cm^{-2})	FF (%)	PCE (%)
PCBM/C60	1.06±0.01 (1.07)	22.77±0.42 (23.20)	79.21±1.26 (80.70)	19.19±0.51 (20.09)
FP-C4/C60	1.05±0.01 (1.07)	21.98±0.82 (22.92)	67.82±2.50 (68.70)	15.70±0.78 (16.90)
FP-C8/C60	1.09±0.01 (1.10)	23.31±0.36 (23.83)	81.57±0.81 (82.76)	20.82±0.44 (21.69)
FP-C12/C60	1.09±0.01 (1.09)	23.00±0.39 (23.36)	80.14±1.13 (81.35)	20.08±0.33 (20.71)

[a]Average values with standard deviation were obtained from 30 devices, the values in parentheses are the parameters of the best device.

Table S4. Photovoltaic parameters of $FAPbI_3$ based PSCs with C60 single layer ETL under AM1.5G illumination[a].

ETL	V_{OC} (V)	J_{SC} (mA cm^{-2})	FF (%)	PCE (%)
C60	1.08±0.01 (1.08)	24.20±0.31 (24.77)	82.18±0.94 (82.60)	21.53±0.49 (22.18)

[a]Average values with standard deviation were obtained from 15 devices, the values in parentheses are the parameters of the best device.

Table S5. Photovoltaic parameters of $FAPbI_3$ based PSCs with PCBM/C60 or FP-C8/C60 bilayer ETL under AM1.5G illumination[a].

ETL	V_{OC} (V)	J_{SC} (mA cm^{-2})	FF (%)	PCE (%)
PCBM/C60	1.09 ±0.02	23.79 ±0.28	80.52 ±1.41	20.81 ±0.41
	(1.10)	(23.89)	(81.28)	(21.41)
FP-C8/C60	1.12 ±0.01	24.17 ±0.39	82.34 ±0.70	22.20 ±0.53
	(1.12)	(24.65)	(83.49)	(23.08)

[a]Average values with standard deviation were obtained from 15 devices, the values in parentheses are the parameters of the best device.

Table S6. TRPL spectra data for pristine CsFAMA perovskite and perovskite coated with PCBM or FP-C8[a].

sample	τ_1 (ns)	A_1 (%)	τ_2 (ns)	A_2 (%)	τ_{avg} (ns)
perovskite	70.33	6.77	378.32	93.23	374.22
perovskite/PCBM	9.03	52.54	74.13	47.46	66.39
perovskite/FP-C4	12.79	9.45	101.80	90.55	100.65
perovskite/FP-C8	2.60	53.41	27.27	46.59	24.84
perovskite/FP-C12	3.29	46.32	56.72	53.68	54.17

[a]All the samples were prepared on quartz. The τ_{avg} was calculated using the equation: $\tau_{avg}=\Sigma A_i\tau_i^2/(\Sigma A_i\tau_i)$.

References

(S1) Tada, T.; Ishida, Y.; Saigo, K. Synthesis and Reactions of 2,2-[60]Fullerenoalkanoyl Chlorides. *J. Org. Chem.* **2006**, *71*, 1633-1639.

(S2) Zhang, X.; Hsu, C.-H.; Ren, X.; Gu, Y.; Song, B.; Sun, H.-J.; Yang, S.; Chen, E.; Tu, Y.; Li, X.; Yang, X.; Li, Y.; Zhu, X. Supramolecular [60]Fullerene Liquid Crystals Formed By Self-Organized Two-Dimensional Crystals. *Angew. Chem. Int. Ed.* **2015**, *54*, 114-117.

(S3) Reddy, M. K.; Varathan, E.; Lobo, N. P.; Roy, A.; Narasimhaswamy, T.; Ramanathan, K. V. Monolayer to Interdigitated Partial Bilayer Smectic C Transition in Thiophene-Based Spacer Mesogens: X-ray Diffraction and ^{13}C Nuclear Magnetic Resonance Studies. *Langmuir* **2015**, *31*, 10831-10842.

(S4) Li, N.; Tao, S.; Chen, Y.; Niu, X.; Onwudinanti, C. K.; Hu, C.; Qiu, Z.; Xu, Z.; Zheng, G.; Wang, L.; Zhang, Y.; Li, L.; Liu, H.; Lun, Y.; Hong, J.; Wang, X.; Liu, Y.; Xie, H.; Gao, Y.; Bai, Y.; Yang, S.; Brocks, G.; Chen, Q.; Zhou, H. Cation and anion immobilization through chemical bonding enhancement with fluorides for stable halide perovskite solar cells. *Nat. Energy* **2019**, *4*, 408-415.

(S5) Hummelen, J. C.; Knight, B. W.; LePeq, F.; Wudl, F.; Yao, J.; Wilkins, C. L. Preparation and Characterization of Fulleroid and Methanofullerene Derivatives. *J. Org. Chem.* **1995**, *60*, 532-538.

(S6) Hexemer, A.; Bras, W.; Glossinger, J.; Schaible, E.; Gann, E.; Kirian, R.; MacDowell, A.; Church, M.; Rude, B.; Padmore, H. A SAXS/WAXS/GISAXS Beamline with Multilayer Monochromator. *J. Phys.: Conf. Ser.* **2010**, *247*,

012007.

(S7) Malliaras, G. G.; Salem, J. R.; Brock, P. J.; Scott, C. Electrical characteristics and efficiency of single-layer organic light-emitting diodes. *Phys. Rev. B* **1998**, *58*, R13411–R13414.

(S8) Bube, R. H. Trap Density Determination by Space‐Charge‐Limited Currents. *J. Appl. Phys.* **1962**, *33*, 1733-1737.

(S9) Kresse, G.; Furthmüller, J. Efficient iterative schemes for ab initio total-energy calculations using a plane-wave basis set. *Phys. Rev. B* **1996**, *54*, 11169-11186.

(S10) Perdew, J. P.; Burke, K.; Ernzerhof, M. Generalized Gradient Approximation Made Simple. *Phys. Rev. Lett.* **1996**, *77*, 3865-3868.

(S11) Blöchl, P. E. Projector augmented-wave method. *Phys. Rev. B* **1994**, *50*, 17953-17979.

(S12) Monkhorst, H. J.; Pack, J. D. Special points for Brillouin-zone integrations. *Phys. Rev. B* **1976**, *13*, 5188-5192.

(S13) Grimme, S. Semiempirical GGA-type Density Functional Constructed with a Long-range Dispersion Correction. *J. Comput. Chem.* **2006**, *27*, 1787-1799.

(S14) Hopfinger, A. J.; Pearlstein, R. A. Molecular mechanics force-field parameterization procedures. *J. Comput. Chem.* **1984**, *5*, 486-499.

(S15) Rappé, A. K.; Casewit, C. J.; Colwell, K. S.; Goddard, W. A.; Skiff, W. M. UFF, a full periodic table force field for molecular mechanics and molecular dynamics simulations. *J. Am. Chem. Soc.* **1992**, *114*, 10024-10035.

(S16) Casewit, C. J.; Colwell, K. S.; Rappé, A. K. Application of a universal force

field to organic molecules. *J. Am. Chem. Soc.* **1992**, *114*, 10035-10046.

(S17) Rappé, A. K.; Goddard, W. A. Charge equilibration for molecular dynamics simulations. *J. Phys. Chem.* **1991**, *95*, 3358-3363.

(S18) Jeng, J.-Y.; Chiang, Y.-F.; Lee, M.-H.; Peng, S.-R.; Guo, T.-F.; Chen, P.; Wen, T.-C. $CH_3NH_3PbI_3$ Perovskite/Fullerene Planar-Heterojunction Hybrid Solar Cells. *Adv. Mater.* **2013**, *25*, 3727-3732.

(S19) Wang, Q.; Shao, Y.; Dong, Q.; Xiao, Z.; Yuan, Y.; Huang, J. Large fill-factor bilayer iodine perovskite solar cells fabricated by a low-temperature solution-process. *Energy Environ. Sci.* **2014**, *7*, 2359-2365.

(S20) Shao, Y.; Xiao, Z.; Bi, C.; Yuan, Y.; Huang, J. Origin and elimination of photocurrent hysteresis by fullerene passivation in $CH_3NH_3PbI_3$ planar heterojunction solar cells. *Nat. Commun.* **2014**, *5*, 5784.

(S21) Chiang, C.-H.; Tseng, Z.-L.; Wu, C.-G. Planar heterojunction perovskite/$PC_{71}BM$ solar cells with enhanced open-circuit voltage via a (2/1)-step spin-coating process. *J. Mater. Chem. A* **2014**, *2*, 15897-15903.

(S22) Azimi, H.; Ameri, T.; Zhang, H.; Hou, Y.; Quiroz, C. O. R.; Min, J.; Hu, M.; Zhang, Z. G.; Przybilla, T.; Matt, G. J.; Spiecker, E.; Li, Y.; Brabec, C. J. A Universal Interface Layer Based on an Amine-Functionalized Fullerene Derivative with Dual Functionality for Efficient Solution Processed Organic and Perovskite Solar Cells. *Adv. Energy Mater.* **2015**, *5*, 1401692.

(S23) Liang, P.-W.; Chueh, C.-C.; Williams, S. T.; Jen, A. K.-Y. Roles of Fullerene-Based Interlayers in Enhancing the Performance of Organometal

Perovskite Thin-Film Solar Cells. *Adv. Energy Mater.* **2015**, *5*, 1402321.

(S24) Nie, W.; Tsai, H.; Asadpour, R.; Blancon, J.-C.; Neukirch, A. J.; Gupta, G.; Crochet, J. J.; Chhowalla, M.; Tretiak, S.; Alam, M. A.; Wang, H.-L.; Mohite, A. D. High-efficiency solution-processed perovskite solar cells with millimeter-scale grains. *Science* **2015**, *347*, 522-525.

(S25) Chiang, C.-H.; Wu, C.-G. Bulk heterojunction perovskite–PCBM solar cells with high fill factor. *Nat. Photonics* **2016**, *10*, 196-200.

(S26) Wu, Y.; Yang, X.; Chen, W.; Yue, Y.; Cai, M.; Xie, F.; Bi, E.; Islam, A.; Han, L. Perovskite solar cells with 18.21% efficiency and area over 1 cm^2 fabricated by heterojunction engineering. *Nat. Energy* **2016**, *1*, 16148.

(S27) Bai, Y.; Dong, Q.; Shao, Y.; Deng, Y.; Wang, Q.; Shen, L.; Wang, D.; Wei, W.; Huang, J. Enhancing stability and efficiency of perovskite solar cells with crosslinkable silane-functionalized and doped fullerene. *Nat. Commun.* **2016**, *7*, 12806.

(S28) Xue, Q.; Bai, Y.; Liu, M.; Xia, R.; Hu, Z.; Chen, Z.; Jiang, X.-F.; Huang, F.; Yang, S.; Matsuo, Y.; Yip, H.-L.; Cao, Y. Dual Interfacial Modifications Enable High Performance Semitransparent Perovskite Solar Cells with Large Open Circuit Voltage and Fill Factor. *Adv. Energy Mater.* **2017**, *7*, 1602333.

(S29) Wolff, C. M.; Zu, F.; Paulke, A.; Toro, L. P.; Koch, N.; Neher, D. Reduced Interface-Mediated Recombination for High Open-Circuit Voltages in $CH_3NH_3PbI_3$ Solar Cells. *Adv. Mater.* **2017**, *29*, 1700159.

(S30) Zhang, F.; Shi, W.; Luo, J.; Pellet, N.; Yi, C.; Li, X.; Zhao, X.; Dennis, T. J.

S.; Li, X.; Wang, S.; Xiao, Y.; Zakeeruddin, S. M.; Bi, D.; Grätzel, M. Isomer-Pure Bis-PCBM-Assisted Crystal Engineering of Perovskite Solar Cells Showing Excellent Efficiency and Stability. *Adv. Mater.* **2017**, *29*, 1606806.

(S31) Xu, G.; Xue, R.; Chen, W.; Zhang, J.; Zhang, M.; Chen, H.; Cui, C.; Li, H.; Li, Y.; Li, Y. New Strategy for Two-Step Sequential Deposition: Incorporation of Hydrophilic Fullerene in Second Precursor for High-Performance *p-i-n* Planar Perovskite Solar Cells. *Adv. Energy Mater.* **2018**, *8*, 1703054.

(S32) Luo, Z.; Wu, F.; Zhang, T.; Zeng, X.; Xiao, Y.; Liu, T.; Zhong, C.; Lu, X.; Zhu, L.; Yang, S.; Yang, C. Designing a Perylene Diimide/Fullerene Hybrid as Effective Electron Transporting Material in Inverted Perovskite Solar Cells with Enhanced Efficiency and Stability. *Angew. Chem. Int. Ed.* **2019**, *58*, 8520-8525.

(S33) Li, M.; Yang, Y.-G.; Wang, Z.-K.; Kang, T.; Wang, Q.; Turren-Cruz, S.-H.; Gao, X.-Y.; Hsu, C.-S.; Liao, L.-S.; Abate, A. Perovskite Grains Embraced in a Soft Fullerene Network Make Highly Efficient Flexible Solar Cells with Superior Mechanical Stability. *Adv. Mater.* **2019**, *31*, 1901519.

(S34) Yao, K.; Leng, S.; Liu, Z.; Fei, L.; Chen, Y.; Li, S.; Zhou, N.; Zhang, J.; Xu, Y.-X.; Zhou, L.; Huang, H.; Jen, A. K.-Y. Fullerene-Anchored Core-Shell ZnO Nanoparticles for Efficient and Stable Dual-Sensitized Perovskite Solar Cells. *Joule* **2019**, *3*, 417-431.

(S35) Ahmad, T.; Wilk, B.; Radicchi, E.; Pineda, R. F.; Spinelli, P.; Herterich, J.; Castriotta, L. A.; Dasgupta, S.; Mosconi, E.; Angelis, F. D.; Kohlstädt, M.; Würfel, U.; Carlo, A. D.; Wojciechowski, K. New Fullerene Derivative as an n-Type

Material for Highly Efficient, Flexible Perovskite Solar Cells of a *p-i-n* Configuration. *Adv. Funct. Mater.* **2020**, *30*, 2004357.

(S36) Li, S.; Fan, K.; Cui, Y.; Leng, S.; Ying, Y.; Zou, W.; Liu, Z.; Li, C.-Z.; Yao, K.; Huang, H. Unravelling the Mechanism of Ionic Fullerene Passivation for Efficient and Stable Methylammonium-Free Perovskite Solar Cells. *ACS Energy Lett.* **2020**, *5*, 2015-2022.

(S37) Wang, K.; Wu, C.; Hou, Y.; Yang, D.; Ye, T.; Yoon, J.; Sanghadasa, M.; Priya, S. Isothermally crystallized perovskites at room-temperature. *Energy Environ. Sci.* **2020**, *13*, 3412-3422.

(S38) Liu, Z.; Siekmann, J.; Klingebiel, B.; Rau, U.; Kirchartz, T. Interface Optimization via Fullerene Blends Enables Open-Circuit Voltages of 1.35 V in $CH_3NH_3Pb(I_{0.8}Br_{0.2})_3$ Solar Cells. *Adv. Energy Mater.* **2021**, *11*, 2003386.

(S39) Su, R.; Xu, Z.; Wu, J.; Luo, D.; Hu, Q.; Yang, W.; Yang, X.; Zhang, R.; Yu, H.; Russell, T. P.; Gong, Q.; Zhang, W.; Zhu, R. Dielectric screening in perovskite photovoltaics. *Nat. Commun.* **2021**, *12*, 2479.